Biomaterials Science

Structured Micro/Nano Materials Synthesized via Electrospray: a Review

Journal:	*Biomaterials Science*
Manuscript ID	BM-REV-08-2020-001313.R1
Article Type:	Review Article
Date Submitted by the Author:	14-Sep-2020
Complete List of Authors:	He, Tengyu; University of California San Diego, Materials Science and Engineering Jokerst, Jesse; University of California San Diego,

Structured Micro/Nano Materials Synthesized via Electrospray: a Review

Tengyu He[1], Jesse V. Jokerst[1,2,3,*]

[1]Materials Science and Engineering Program, University of California, San Diego, La Jolla, CA 92093, USA

[2]Department of NanoEngineering, University of California, San Diego, La Jolla, CA 92093, USA

[3]Department of Radiology, University of California, San Diego, La Jolla, CA 92093, USA

[*]jjokerst@ucsd.edu

Abstract

The development of synthetic methods for micro/nano materials with precisely controlled structures, morphologies, and local compositions is of great importance for the advancement of modern nanotechnology. The electrospray method is a "platform" approach for the preparation of a broad range of micro-/nanostructures; electrospray is simple and scalable. This review summarizes recent research on the micro-/nanostructures prepared via the electrospray route. These include spherical structures (e.g. simple, porous, Janus, and core-shell particles), non-spherical structures (e.g. red blood cell-like and spindle-like particles, multi-compartment microrods, 2D holey nanosheets, and nanopyramids), and assembled structures. The experimental details, underlying physical/chemical principles, and key benefits of these structures are comprehensively discussed. The effects and importance of nozzle design, properties of feeding solutions (e.g. concentration of solute, polymer additives, solvent/nonsolvent combinations), working environment (e.g. temperature and humidity), and types of collection media are highlighted.

1. Introduction

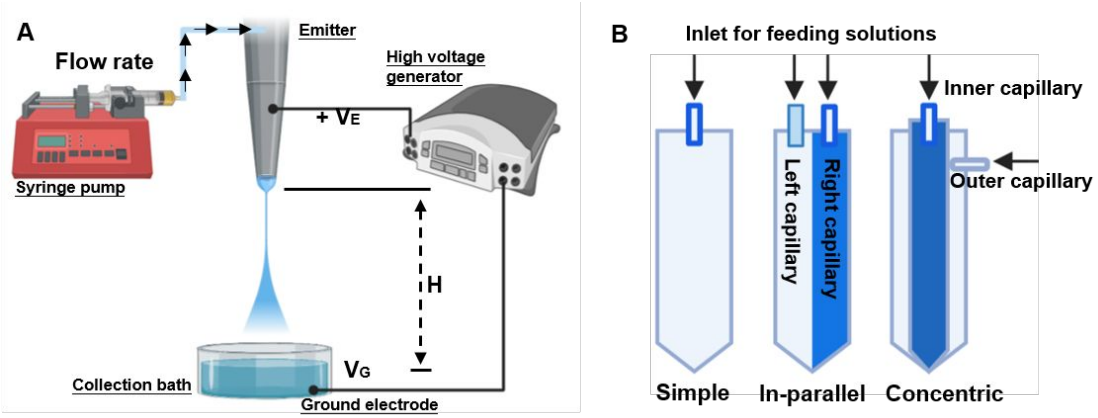

Figure 1. Schematic illustration of the experimental setup for electrospray. A) In a basic electrospray experiment, the liquid is continuously supplied by a syringe pump, and the electric field is generated by a high-voltage generator connecting the emitter and a ground electrode. V_E is the emitter voltage and V_G is the ground voltage. H is the working distance defined as the distance between the nozzle tip and the ground electrode. **B)** The emitter is a metal nozzle that can be categorized into three types: simple type (single capillary), in-parallel type (multiple capillaries), and concentric type (multiple capillaries).

Electrospray is an electrohydrodynamic atomization method that generates fine charged droplets by charging the liquid flowing through a nozzle with an applied electric field. The as-generated droplets are further solidified to form the final particle products. The electrohydrodynamic atomization phenomenon was observed by Nollet in the 17th century for the first time[1, 2]. He described that "a person, electrified by connection to a high-voltage generator, would not bleed normally if he were to cut himself; blood would spray from the wound". After that, Rayleigh (1882) defined the limit on the charge in a droplet[3], Zeleny (1914) reported various possible spraying modes[4], and Taylor (1964) mathematically defined the cone shape at the capillary tip[5]. Following the first experiment on electrospray ionization mass spectrometry (ESI-MS) by J.B. Fenn (1984)[6], ESI-MS has become a very important analysis approach in chemistry and biology for unknown molecules. Since the 1990s, electrospray has begun to be widely used to produce micro-/nanostructured materials[7].

Controlling the structures, morphologies, and local compositions of materials at the micro/nano scale is of fundamental scientific interest[8-11]. This is because of the tight relationship between desired functions of the materials and its structures, morphologies, and compositions. There are many micro/nano materials with controlled structures, morphologies, and local compositions prepared via self-assembly[12-15], emulsion-based method[16-20], template-assisted approach[21-23], layer by layer polyelectrolyte coating[24-26], and electrospray[27-37]. For simplicity, a single "platform method" that can be sufficiently versatile to prepare most structures is highly desired. Electrospray is such a platform. Electrospray-related review papers are available for the following sub-topics: fundamental physics and modeling of electrospray[7, 38, 39], experimental setup[38], the selection of solvents for electrospray[40], preparation of materials via electrospray for biomedical[38, 41] and foods[42] applications, and co-axial electrospray[41]. However, a comprehensive and current text that evaluates this platform system with an eye to theory and applications is missing. This review fills that need. More specifically, this text describes the structures, morphologies, and local compositions of materials that can be controlled at the micro/nano scale via electrospray route. This review is divided into four

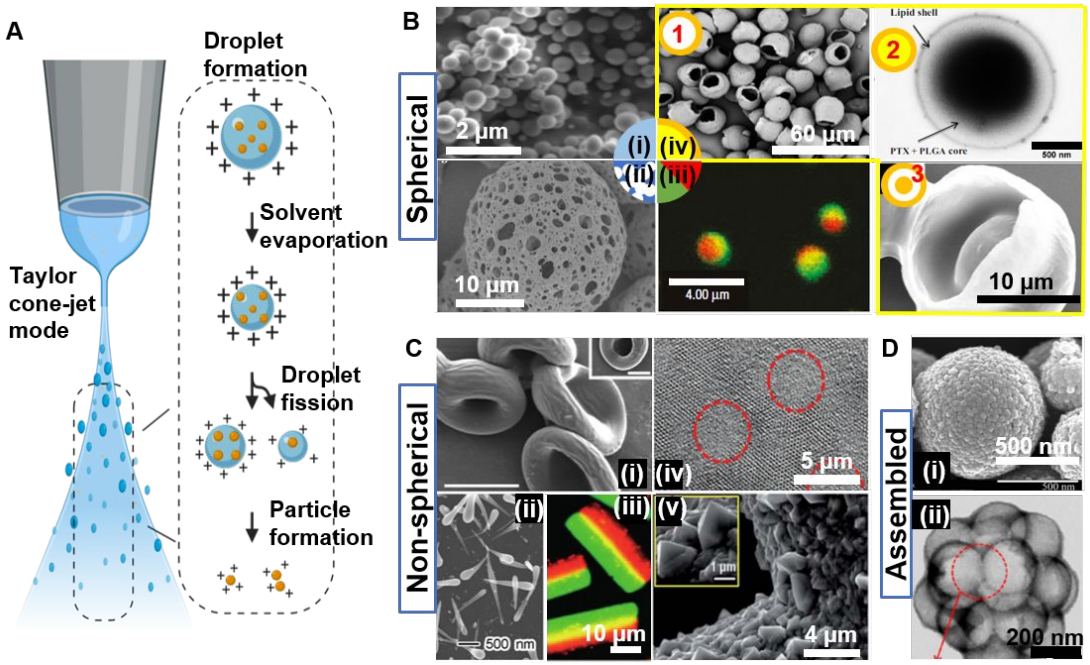

Figure 2. Schematic illustration of the Taylor cone-jet mode electrospray process and SEM images of possible micro/nano structures prepared via the electrospray route. A) A cone with a jet at its apex appears when the applied voltage reaches the critical value called onset voltage. The jet then breaks into charged droplets. Smaller droplets are formed during fission, and particles are formed when the droplets dry. SEM/optical microscopy images of **B)** spherical particles ((i) simple particles[51], (ii) porous particles[27], (iii) Janus particles[52], (iv) core-shell particles including subtypes of hollow[28], core-shell[53], and yolk-shell particles[54]), **C)** non-spherical particles ((i) RBC-like particles[37], (ii) spindle-like particles[55], (iii) multi-compartment microrods[56], (iv) holey nanosheet[57], (v) nanopyramids[32]), **D)** assembly of primary building blocks[29,33]. **B(i)** is adapted with permission from REF. 51. Copyright (2015) American Chemical Society. **B(ii)** is adapted with permission from REF. 27. Copyright (2013) Springer Nature. **B(iii)** is adapted with permission from REF. 52. Copyright (2005) Springer Nature. **B(iv1)** is adapted with permission from REF. 28. Copyright (2017) American Chemical Society. **B(iv2)** is adapted with permission from REF. 53. Copyright (2019) Elsevier Ltd. **B(iv3)** is adapted with permission from REF. 54. Copyright (2017) American Chemical Society. **C(i)** is adapted with permission from REF. 37. Copyright (2009) National Academy of Sciences. **C(ii)** is adapted with permission from REF. 55. Copyright (2007) Elsevier Ltd. **C(iii)** is adapted with permission from REF. 56. Copyright (2009) John Wiley & Sons Inc. **C(iv)** is adapted with permission from REF. 57. Copyright (2018) John Wiley & Sons Inc. **C(v)** is adapted with permission from REF. 32. Copyright (2019) Royal Society of Chemistry. **D** is adapted with permission from REF.29. Copyright (2011) American Chemical Society and REF. 33. Copyright (2013) American Chemical Society.

sections. In section 2, the basic experimental setup and fundamental theories of electrospray are briefly discussed. In section 3, electrospray experimental details for the preparation of various structured micro/nano particles are described. More importantly, representative work is selected to explain key physical/chemical mechanisms and how each refined structure/composition benefits specific applications. Our main goal is to understand how the process parameters, physicochemical properties of the solvents and solutes, droplet charge and solute charge, and the solute concentration affect the structures, size, and morphologies of the as-prepared materials. In section 4, the main conclusions are drawn and perspectives for current challenges and future directions in this field are

highlighted.

2. Basic setup and fundamental theories

A brief discussion on the basic experimental setup of electrospray and fundamental theories is given in this section. A more detailed review of electrospray experimental setup and theories can be found in the literature[2, 7, 11, 39, 42]. In a basic electrospray experiment (**Figure** 1A), the liquid is continuously supplied by a syringe pump, and the electric field is generated by a high-voltage source connecting the emitter and a ground electrode. The emitter is usually a simple capillary metal nozzle, although more advanced designs such as concentric and in-parallel multi-capillary nozzles (**Figure** 1B) exist for more specific applications, such as the synthesis of core-shell and Janus micro/nano particles, as discussed in section 3 in detail.

2.1 Taylor cone-jet mode and onset voltage

As the applied voltage increases, the spraying mode changes from dripping mode to spindle mode, Taylor cone-jet mode, and multi-jet mode[43-45]. Taylor cone-jet mode[5] is most favored for nano/micro particle fabrication because it offers stable generation of more monodispersed droplets with sizes ranging from a few hundred nanometers to micrometers[2].

The droplet and particle formation process under Taylor cone-jet mode is presented in **Figure** 2A. When the applied voltage reaches the so-called onset voltage, the electric field is strong enough to deform the liquid meniscus into a cone with a jet at its apex. The onset voltage is given by[39, 46, 47],

$$V_{critical} \approx \sqrt{\frac{2\gamma R\cos\theta}{\varepsilon_0}\ln\left(\frac{4l}{R}\right)}$$

where θ is the semi-cone angle, R is the capillary radius, γ is the solution surface tension, l is the distance between the capillary and the ground electrode, and ε_0 is the permittivity of vacuum. This expression is valid when the electrode separation (l) is much larger than the radius of the nozzle (r_c).

2.2 Rayleigh limit

The jet disintegrates and generates primarily charged droplets. As the primarily charged droplets fly through the electric field, the evaporation of solvents leads to a decrease in droplet size and an increase in surface charge density. When the surface charge density reaches a limit known as the Rayleigh limit, the overall electrostatic repulsive force overcomes the surface tension forces resulting in the fission of the primary droplets and generation of smaller secondary droplets. Charged particles are generated after the complete evaporation of solvents. The size at which the droplet with a charge q, and a surface energy per unit area, σ, breaks into smaller droplets is given by[3, 48, 49]

$$r_{Rayleigh} \approx \left(\frac{q^2}{64\pi^2\varepsilon_0\sigma}\right)^{1/3}$$

2.3 Scaling law

The beauty of electrospray under the Taylor cone-jet mode is that the jet diameter can be precisely

estimated by the so-called scaling law given liquid properties and electrospray operation parameters, which provides useful guidance on the size control of the as-formed particles because the size of particles is proportional to the jet diameter. The specific mathematic expression for the scaling law varies depending on dominant conditions and liquid properties[39]. For example, when inertia stress and electrostatic suction are assumed to be dominant forces and non-polar liquid with low viscosity is to be modeled, the scaling law is found to be[50]:

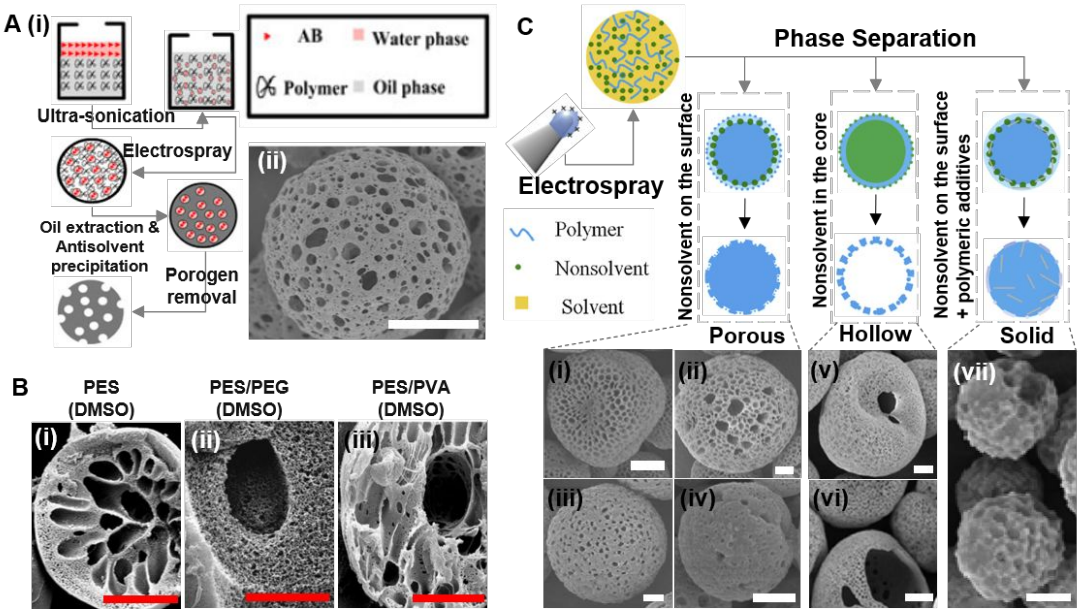

Figure 3. Preparation and characterization of porous particles via A) microemulsion-assisted electrospray (MEAES) and B)-C) nonsolvent-assisted electrospray (NSAES). A) Porous particles prepared via MEAES process. (i) MEAES starts with the preparation of a bulk microemulsion solution via ultra-sonication, which is followed by electrospray, oil extraction & antisolvent precipitation, and porogen removal. The electrospray step creates primary micro/nano droplets that contain secondary microemulsion droplets of porogens. Porogen used here is ammonium bicarbonate (AB). (ii) SEM image of porous poly-L-lactide (PLLA) microparticles obtained after removing porogens. Scale bar, 10 μm[27]. Adapted with permission from REF. 27. Copyright (2013) Springer Nature. **B)** Porous particles prepared via NSAES process with nonsolvent being introduced in the collection bath. SEM images of three different porous polyethersulfone (PES) structures formed by adjusting the polymer additives in the feeding PES/ dimethyl sulfoxide (DMSO) solution: (i) macrovoids surrounded by a dense porous shell (MDPS) (without polymeric additives), (ii) single macroviod surrounded by a dense porous shell (SMDPS) (with polyethylene glycol (PEG)), and (iii) parallel macrovoid (PM) (with poly(vinyl alcohol) (PVA)). Scale bar, 5 μm[74]. Adapted with permission from REF. 74. Copyright (2010) Springer Nature. **C)** Porous particles prepared via NSAES process with nonsolvent being introduced in the feeding solution. SEM images of porous polymethylmethacrylate (PMMA) structures based on different nonsolvents and/or polymeric additives: (i) butanol, (ii) pentanol, (iii) TEOS, (iv) cyclohexanol, (v-vi) ethanol and propanediol, and (vii) pentanol with polyvinylpyrrolidone (PVP). Scale bar, 1 μm[75]. Adapted with permission from REF. 75. Copyright (2014) Elsevier Ltd.

$$D_j \approx \left(\frac{\rho \varepsilon_0 Q^3}{\gamma K}\right)^{1/6}$$

where D_j is the jet diameter, ρ is the density, ε_0 is the permittivity of vacuum, K is the electrical

conductivity, γ is the surface tension, and Q is the flow rate of the liquid. In other words, the jet diameter is proportional to liquid density, flow rate, and inversely proportional to electrical conductivity and surface tension.

3. Structured micro/nano materials and their applications

For simplicity, micro/nano structures that can be prepared via electrospray are grouped into three main categories: spherical (**Figure** 2B), non-spherical (**Figure** 2C), and assembled structures (**Figure** 2D). Specifically, the spherical type includes simple (**Figure** 2B(i))[51], porous (**Figure** 2B(ii))[27], Janus (**Figure** 2B(iii))[52], and core-shell particles (**Figure** 2B(iv))[28, 53, 54]. Non-spherical structures include red blood cell-like (RBC-like) (**Figure** 2C(i))[37] and spindle-like particles (**Figure** 2C(ii))[55], multi-compartment microrods (**Figure** 2C(iii))[56], 2D holey nanosheets (**Figure** 2C(iv))[57], and nanopyramids (**Figure** 2C(v))[32]. The assembled structure is the assembly of primary building blocks (**Figure** 2D)[29, 33]. In this section, we will discuss in detail the synthesis and underlying formation mechanism for each of these categories (see Table 1 for the experimental details of the synthesis of selected micro/nano structures). The application benefits from such structures will also be highlighted. A review of the synthesis of structured particles using other methods can be found elsewhere[8].

3.1 Spherical structures

3.1.1 Porous particle

Porous particles have external pores on the surface and/or internal pores in the core enabling large specific surface area and low density. Such properties are critical for many bio-applications, such as tissue regeneration scaffolds[58-61], high-speed protein chromatography[62-64], carriers for biomacromolecules[65-68], pulmonary drug delivery[69-72], and gastric drug delivery[73]. For example, for tissue regeneration, a scaffold with a highly porous structure and interconnected pores is beneficial for sufficient cell seeding and in- and out-transport of nutrients and oxygen necessary for subsequent cell proliferation and differentiation[58].

Porous structures can be obtained via two sub-types of electrospray method: microemulsion-assisted electrospray (MEAES)[27] and nonsolvent-assisted electrospray (NSAES)[74, 75]. In the MEAES process, a bulk microemulsion solution is prepared first, which is used for subsequent electrospray to create primary micro/nano droplets that contain secondary microemulsion droplets of porogens. Porous microparticles are obtained after removing the porogens (**Figure** 3A(i)). Methotrexate (MTX)-loaded and highly-porous poly-L-lactide (PLLA) microspheres have been prepared by this method (**Figure** 3A)[27]. MTX in dimethyl sulfoxide (DMSO) solution and PLLA in dichloromethane (DCM) solution were mixed with ammonium bicarbonate (AB) aqueous solution, which was emulsified with Pluronic F127 (PF127) as the emulsion stabilizer. The as-prepared emulsion was electrosprayed into an ethanol bath. Ethanol acted as an antisolvent for the extraction of DMSO and DCM causing the co-precipitation of PLLA and MTX and thus forming microspheres with AB aqueous micro-droplets uniformly embedded. AB aqueous micro-droplets were removed by lyophilization forming MTX-loaded PLLA microparticles with a mean diameter of 25 μm, mass median aerodynamic diameter of 3.1 ± 0.2 μm, and porosity of 81.8 % (**Figure** 3A(ii)).

Porous structures can also be prepared through the NSAES method. Generally, upon the

introduction of a nonsolvent (a solvent in which a polymer has a very low solubility) to a polymer-solvent system, polymer-lean phases are separated from polymer-rich phases due to the low solubility of a polymer in its nonsolvent. This process is termed as nonsolvent-induced phase separation (NIPS). Following NIPS and curing of the polymer, pores will form at the polymer-lean phases. The nonsolvent can be introduced either in the collection bath (**Figure** 3B)[74] or in the feeding solution for electrospray (**Figure** 3C)[75].

Porous polyethersulfone (PES) microparticles were prepared by electrospraying PES/DMSO to a nonsolvent collection bath (water) (**Figure** 3B)[74]. Exchange of solvent (DMSO) and nonsolvent (water) initiated the NIPS process and formed the pores. By varying the polymeric additives in the feeding PES/DMSO solution, three types of structures were prepared: macrovoids surrounded by a dense porous shell (MDPS) (without polymeric additives) (**Figure** 3B(i)), single macroviod surrounded by a dense porous shell (SMDPS) (added with polyethylene glycol (PEG)) (**Figure** 3B(ii)), and parallel macrovoid (PM) (added with PVA) (**Figure** 3B(iii)). The formation of the MDPS structure is the result of the difference in the nonsolvent-solvent exchange rate along the radius direction. As the nonsolvent-solvent exchange rate decreases from the water bath-droplet interface to the droplet core, the phase separation changes from instantaneous separation (surface) to delayed separation (core) accordingly. Instantaneous phase separation was believed to form small pores while delayed phase separation will result in the growth of a macrovoid. When PEG was added to PES/DMSO, the internal pore structure changed from MDPS to SMDPS. This was attributed to the high affinity of PEG to water, which can cause a comparable nonsolvent-solvent exchange rate within the entire droplet. Meanwhile, as PEG preferentially transferred outwardly, an elliptical cavity was left in the innermost. More aligned macrovoids can be created by replacing PEG with PVA, which has poor solubility in DMSO but a high affinity to water. Such a low solubility in DMSO may lead to rapid phase separation of PVA at the beginning of electrospray. As-formed PVA microphases may be elongated and oriented during rapid spinning jet extension. Because PVA also has a high affinity to water, once the droplet was immersed in the water bath, faster nonsolvent-solvent exchange was believed to occur around oriented PVA microphases leading to parallel microvoids. The appearance of an elliptical cavity was attributed to the same reason as discussed in the case of PEG.

Polymethylmethacrylate (PMMA) microspheres were fabricated by NSAES with nonsolvent introduced to the initial feeding polymer solution (**Figure** 3C)[75]. A solution of PMMA/DCM/nonsolvent was electrosprayed, and microspheres were collected on an aluminum foil. By simply varying the use of nonsolvents and/or polymeric additives, three types of microspheres were prepared: porous sphere with a solid core (PSSC) (**Figure** 3C(i-iv)), a porous sphere with a hollow core (PSHC) (**Figure** 3C(v-vi)), and solid sphere with a dented but non-porous surface (SSDS) (**Figure** 3C(vii)). Generally, the structure is mainly determined by nonsolvent properties including the solubility parameter, surface tension, and viscosity. PSSC was formed when a nonsolvent with surface tension lower than that of PMMA was used such as butanol (**Figure** 3C(i)), pentanol (**Figure** 3C(ii)), TEOS (**Figure** 3C(iii)), and cyclohexanol (**Figure** 3C(iv). PSHC was favored by a nonsolvent with surface tension higher than that of PMMA such as propanediol (**Figure** 3C(v-vi). A nonsolvent with surface tension lower than that of the polymer tends to escape to the exterior surface leaving a solid polymer in the core. On the contrary, one with surface tension higher than the polymer prefers to occupy the core creating a void core after evaporation. The morphology

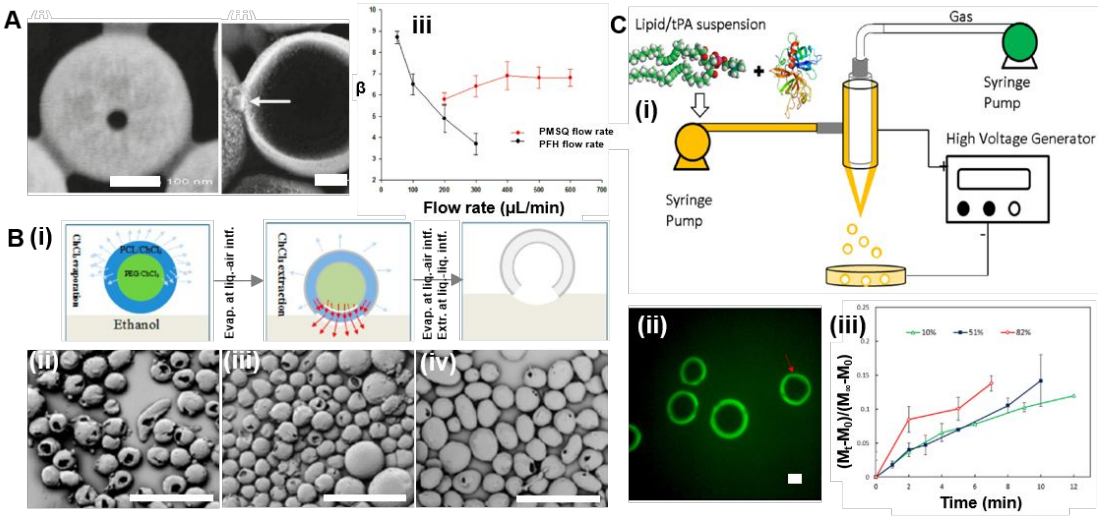

Figure 4. Preparation and characterization of core-shell particles with air-core via co-axial electrospray. A) polymethylsilsesquioxane (PMSQ) hollow particles with a hole on the surface. (i-ii) SEM images of PMSQ hollow particles showing a hole on the surface. Scale bar, 100nm. (iii) Plot showing that the ratio of microsphere diameter/pore diameter decreases/increases as the flow rate of shell-forming PMSQ and core-forming perfluorohexane (PFH) liquid increases[34]. Adapted with permission from REF. 34. Copyright (2010) American Chemical Society. **B)** polycaprolactone (PCL) hollow microspheres with a single hole in the surface. (i) Schematic illustration of the formation of hollow PCL microspheres with a single hole in the surface due to the solvent evaporation and extraction. (ii-iv) SEM images showing the effect of core fluid flow rate on the size of surface hole. It decreases as the core flow rate decreases from 0.5 to 0.2 and 0.05 mL/h. Scale bar, 65 μm[28]. Adapted with permission from REF. 28. Copyright (2017) American Chemical Society. **C)** Tissue plasminogen activator (tPA)-loaded phospholipid microbubbles. (i) Schematic illustration of coaxial electrospray process for the preparation of tPA-loaded phospholipid microbubbles. (ii) Optical microscopy image of tPA-loaded phospholipid microbubbles. Scale bar, 50 μm. (iii) tPA release profile when exposed to an ultrasound at various intensities (10%, 51%, and 82%) with 200 rpm shaking. The initial tPA volume fraction is 0.1[81]. Adapted with permission from REF. 81. Copyright (2017) Elsevier Ltd.

of the surface pores also strongly depends on the viscosity of the nonsolvent. A nonsolvent with low viscosity such as butanol and pentanol has a higher diffusion rate and thus faster nucleation and growth during the NIPS process—this favors the formation of large and continuous pores (**Figure** 3C(i-ii)). In contrast, a nonsolvent with a higher viscosity will result in smaller pores and lower pore density as shown in the case of TEOS and cyclohexanol (**Figure** 3C(iii-iv)). Interestingly, such porous and/or hollow structures will even disappear when polymeric additive, i.e., PVP, was added into the solution (**Figure** 3C(vii)). This loss of pores is because PVP is soluble in both DCM and the nonsolvent. PVP preferably exists in the nonsolvent. The PMMA-lean phase in the NIPS process prevents pore nucleation and growth.

In brief, the pore structure, size, and density can be finely tuned during the electrospray process by a careful selection of the porogen (in the MEAES route) and the type of polymers, non-solvents, and polymer additives (in the NSAES route). As mentioned before, the porous structure is very important for specific drug delivery applications. However, the repeatability of pore formation using these techniques with drug loading has yet to be demonstrated. This is not a trivial issue because the addition of drugs to the original polymer and solvent systems can significantly change the

physicochemical properties governing the pore formation, and the current mechanisms may fail.

3.1.2 Core-shell particle

Core-shell particles with distinct compartments make it possible to contain multiple components in a single particle, which has been desired for many applications such as actuated/programmed/controlled release of drugs[76-78], delivery of materials sensitive to applied environments[31, 79], and co-administration of drugs with synergistic effect[80]. Co-axial electrospray is an extremely simple method for the preparation of the core-shell structure. In co-axial electrospray, a concentric nozzle with multiple compartments is used (**Figure** 1B). Desired materials are fed to each of these compartments in different liquid supplies, giving droplets containing primary droplets that are also co-axially arranged. Core-shell particles are formed once these droplets are solidified. The number of shell layers can be facilely controlled by adding the number of compartments in the nozzle. Depending on the state of the core materials, we divide core-shell particles into three subtypes: air-core, liquid-core, and solid-core, which will be reviewed as follows.

1) Air-core

Core-shell particles with an air core can be a hollow structure with[28, 34], or without[81] a hole on the surface. The use of coaxial electrospray for the synthesis of the hollow microsphere with a single hole in its shell has been demonstrated with different polymer shell materials (**Figure** 4A and B) [28, 34]. In the first case, polymethylsilsesquioxane (PMSQ) was used as the shell material encapsulating a core of a volatile liquid, perfluorohexane (PFH), which was subsequently evaporated resulting in the hollow structure (**Figure** 4A (i-ii))[34]. The ratio of microsphere diameter/pore diameter was found to be highly tunable. As the flow rate of shell-forming PMSQ and core-forming PFH increases, this ratio decreases, and increases, respectively (**Figure** 4A (iii)). The surface hole formation was attributed to the evaporation flux of PFH.

Similar hollow polycaprolactone (PCL) microspheres with a single hole on the surface were prepared from coaxial electrospray of PEG/PCL core/shell solution in chloroform using an ethanol bath as the collection medium (**Figure** 4B). The size of the surface hole was found to be proportional to the flow rate of the core solution (**Figure** 4B(ii-iv)) [28]. It was proposed that the dissolving of PCL and chloroform extraction by ethanol at the sphere/liquid interface was the main reason for the formation of hollow and single-hole structure. For both of the above research reports, proposed mechanisms should be verified by further control experiments. For example, in the case of PMSQ hollow particles, if the volatility of the core solvent is the true reason for the formation of the hole structure, then one can expect no hole formation when the core solvent is replaced by a non-volatile system. In the case of PCL hollow particles good control is needed to verify this mechanism and use a polymer that cannot be dissolved in ethanol; there should be a core solvent immiscible with ethanol. Meanwhile, one should investigate the possibility of preparing similar structures with other polymer materials using these techniques so that such structures can be exploited for a specific application.

Drug (tPA, tissue plasminogen activator)-loaded phospholipid microbubbles were prepared by replacing the liquid with a gas source for the core fluid in coaxial electrospray (**Figure** 4C)[81]. The tPA release rate can be well controlled by the applied ultrasound intensity (**Figure** 4C(iii)). The co-administration of microbubbles (without tPA) and tPA can enhance the efficiency of thrombolysis treatment but its efficacy is still limited by the narrow therapeutic window of tPA to avoid

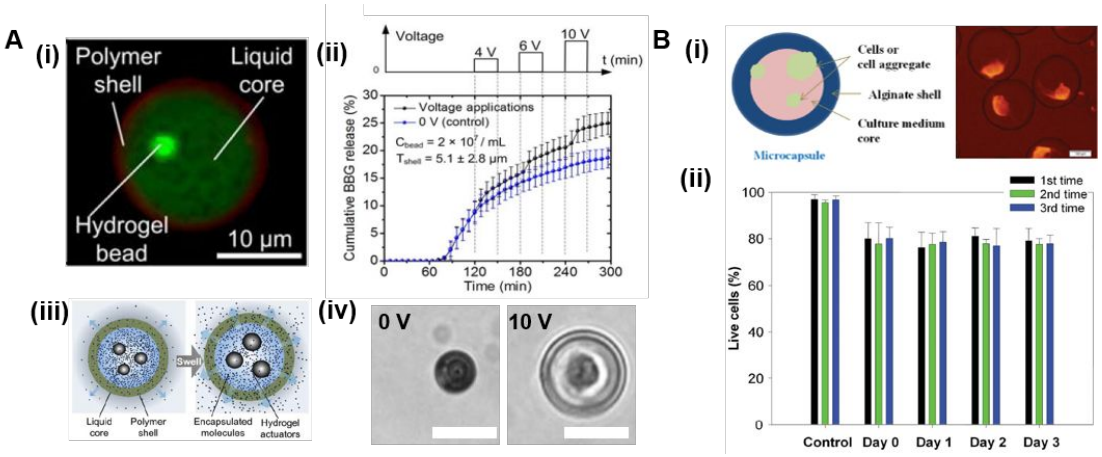

Figure 5. Preparation and characterization of core-shell particles with liquid-core via co-axial electrospray. **A)** Poly(D-lactic acid) (PDLA) stimuli-responsive core-shell microcapsule. (i) Fluorescent image. (ii) Cumulative brilliant blue G dyes (BBG)release from two identical samples of the microcapsules (ID =16.5±3.5 μm; T_{shell} =5.1±2.8 μm; C_{bead} =2×107/mL), responding to two different applied square voltages. (iii) Schematic illustration of the swelling process upon voltage stimuli. (iv) Optical microscopy images of the swelling process under applied voltages. Scale bar, 5 μm[76]. Adapted with permission from REF. 76. Copyright (2013) IEEE. **B)** Cells-encapsulated alginate microcapsule. (i) Schematic illustration and fluorescent microscopy image of cells-encapsulated alginate microcapsule. Scale bar, 100 μm. (ii) Percentage of live cells with prolonged storage time in the microcapsule[31]. Adapted with permission from REF. 31. Copyright (2015) John Wiley & Sons, Inc.

hemorrhage[82, 83]. In comparison, this ultrasound triggerable tPA-loaded microbubble enables controlled and localized tPA drug release and thus provides a promising therapeutic tool for combined treatment of ischemic stroke. To further evaluate the practical usefulness of this material, it should be studied for long-term stability against air-leakage and collapse of the structure without ultrasound triggers.

2) Liquid-core

Encapsulating a liquid in a protective solid shell makes possible many applications based on the liquid component. [76] applied coaxial electrospray to the fabrication of a stimuli-responsive core-shell microcapsule, which contains a poly(D-lactic acid) (PDLA) shell and liquid core with voltage-responsive hydrogel beads and brilliant blue G dyes (BBG) (**Figure** 5A(i)). Responding to external electric fields, the embedded hydrogel beads swell (**Figure** 5A(iii-iv)) and regulate the internal pressure of the liquid core. As a result, the release rate of encapsulated BBG can be remotely controlled (**Figure** 5A(ii)).

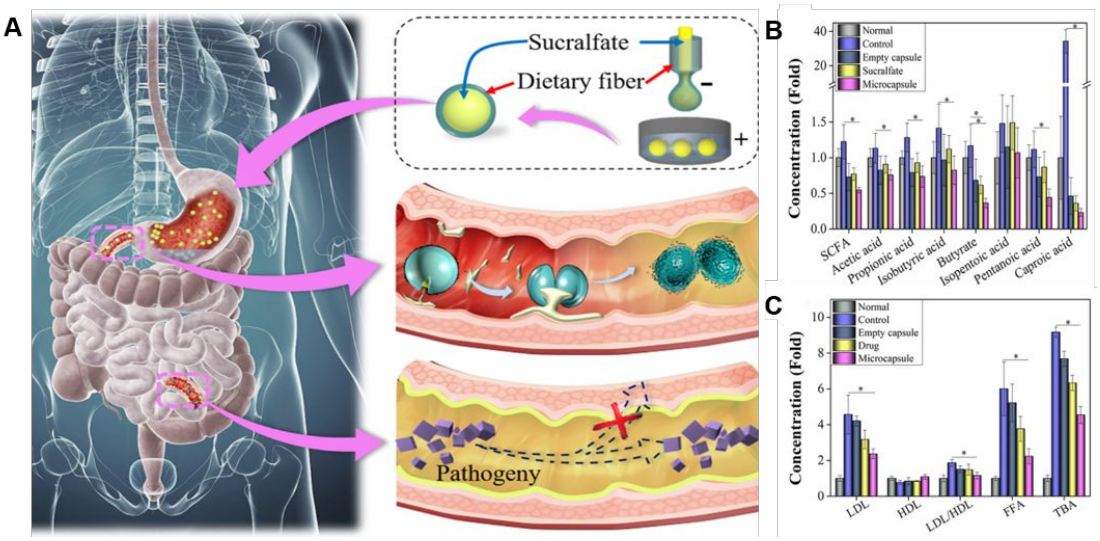

Figure 6. Preparation and characterization of core-shell particles with liquid-core via co-axial electrospray continued. A) Schematic illustration of the coaxial electrospray process, particle structure, and formation process of biomimetic intestinal barrier upon release of sucralfate core encapsulated in dietary fiber shell. **B)** Concentration of short chain fatty acids and **C)** fat metabolism factors measured in rat blood after the rat was treated with a high fat diet and microcapsules[79]. Adapted with permission from REF. 79. Copyright (2019) Science China Press.

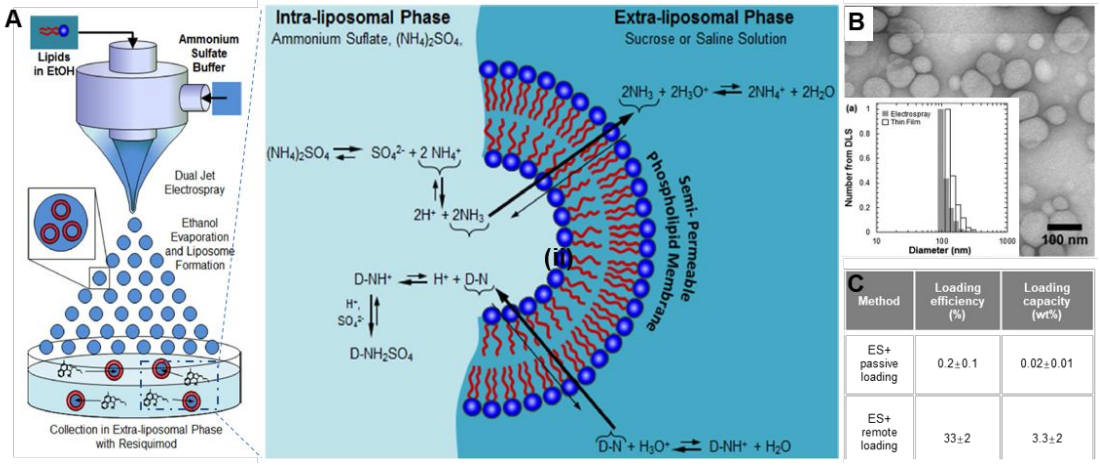

Figure 7. Preparation and characterization of core-shell particles with liquid-core via co-axial electrospray continued. A) Schematic illustration of co-axial electrospray combined with remote loading process in the collection medium for the preparation of drug-loaded liposomes. **B)** SEM image and DLS characterization of as-prepared liposomes and table summarizing the loading efficiency and capacity of drugs[84]. Adapted with permission from REF. 84. Copyright (2016) American Chemical Society.

Delivery of live cells becomes possible with a core-shell structure. A microsphere less than 300 μm containing a core of live cells in liquid culture and an alginate hydrogel shell was fabricated using coaxial electrospray (**Figure** 5B(i))[31]. The thickness of the core and shell can be easily controlled by the core and shell flow rates; 80% viability of encapsulated cells was retained even after 3 days in culture (**Figure** 5B(ii)), which suggests that this core-shell structure enables sufficient nutrients and oxygen supply. This opens up exciting applications including cell delivery, imaging, and diagnosis.

The core-shell structure is also beneficial for the delivery of liquid therapeutic agents that are

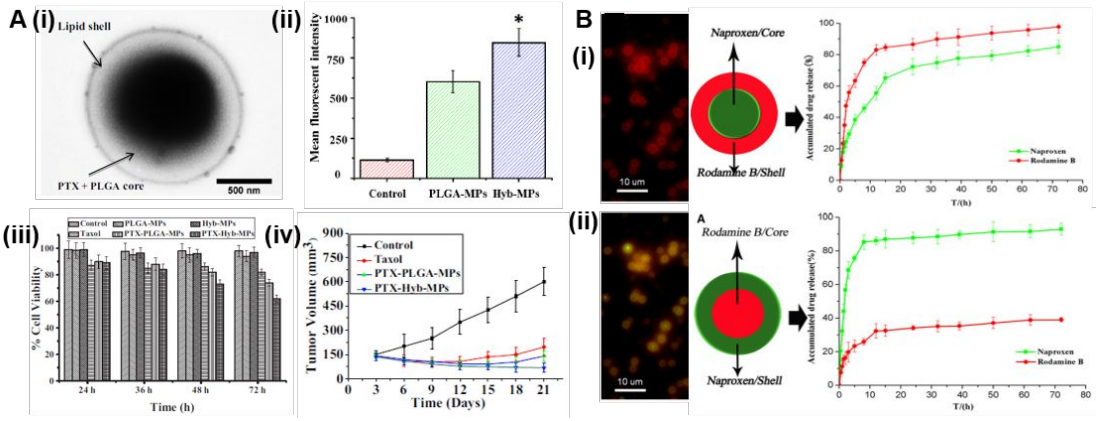

Figure 8. Preparation and characterization of core-shell particles with solid-core. A) PTX-loaded PLGA core-lipid shell microparticles. **(i)** TEM image of paclitaxel (PTX)-loaded core-shell particles showing the lipid shell and poly (lactic acid-co-glycolic acid) (PLGA) core. (ii) The mean fluorescent intensity of cells without treatment (control) and treated with fluorescent labeled PTX-PLGA microparticles (PLGA-MPs) or fluorescent labeled PTX-loaded PLGA core-lipid shell microparticles (Hyb-MPs). The results show that PTX-loaded PLGA core-lipid shell microparticles have the maximum cell uptake. (iii) Cytotoxicity of various "drug" treatments on SKOV-3 cells at different time point of exposure showing that PTX-loaded PLGA core-lipid shell particles demonstrate the optimal cell cytotoxicity. (iv) The change in tumor volume in treated mice as a function of time after a single local injection with PTX equivalent dose of 20 mg/kg[53]. Adapted with permission from REF. 53. Copyright (2019) Elsevier B.V. **B)** Chitosan core-PVP shell particles. Optical microscopy images and drug release profile of chitosan core-PVP shell particles with (i) naproxen (green) in the core and rhodamine B in the shell and (ii) naproxen (green) in the shell and rhodamine B in the core[77]. Adapted with permission from REF. 77. Copyright (2013) Springer Nature.

sensitive to bio-environments. Bioactive mucosal adhesives such as sucralfate and its derivatives are good protective gel-forming agents for ulcer healing, prevention of bleeding, and inhibition of acid invasion. However, they are not stable in the digestive tract and cannot disperse continuously on the intestine. This was solved by encapsulation of sucralfate in a dietary-fiber shell through co-axial electrospray (**Figure** 6A)[79]. Upon release from this core-shell microsphere, sucralfate can form a stable and continuous gelling barrier on the mucosa of the intestine. This biomimetic barrier was proven to be effective in blocking luminal contents of the intestine as indicated by a significantly lower amount of short-chain fatty acids (**Figure** 6B) and fat metabolism factors in rat blood (**Figure** 6C) when the rat was treated with this microsphere in a high-fat diet.

A core-shell structure with a liquid shell can also serve as a micro/nano reactor for in-situ reactions. In one study, co-axial electrospray was combined with remote loading to achieve scalable one-step encapsulation of drugs in liposomes (**Figure** 7)[84]. Co-axial electrospray was conducted with lipids in ethanol as the core fluid and ammonium sulfate buffer as the shell fluid. Lipids assembled in the micro/nano aqueous droplets formed by electrospray, which subsequently entered a collection dish with resiquimod (drug) in PBS, and remote loading of the drug occurred via a series of in-situ reactions controlled by the pH difference between intra- and extra-liposomal phase (**Figure** 7A). The remote loading approach improved drug loading efficiency and capacity in liposomes (**Figure** 7C) while electrospray resulted in better control over the size and size distribution (**Figure** 7B).

One common and unsolved question in all of the studies in this section is how the shell materials

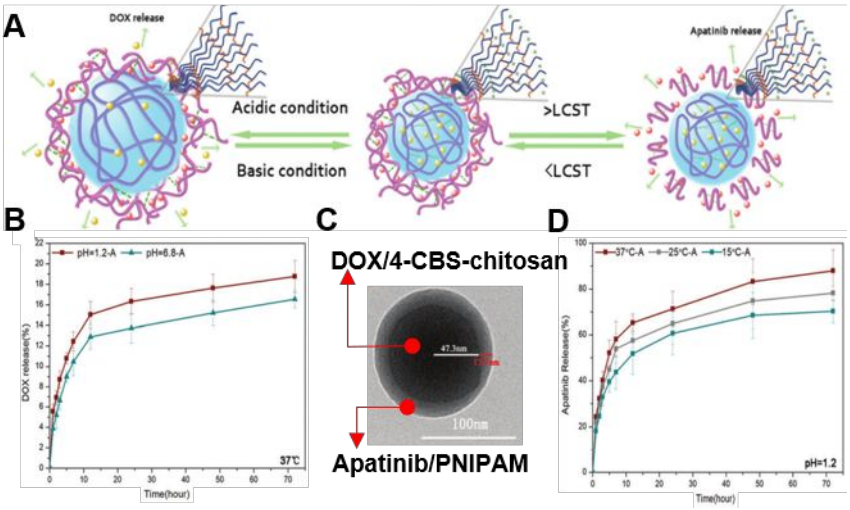

Figure 9. Preparation and characterization of core-shell particles with solid-core continued. 4-CBS-chitosan core and poly(nisopropylacylamide) (PNIPAM) shell particles. A) Schematic illustration of the structure and working mechanism of thermo/pH dual-responsive core–shell particle. This step consists of a PNIPAM shell containing apatinib and chitosan containing doxorubicin (DOX). The PNIPAM shell and 4-CBS-chitosan core are thermo- and pH-sensitive, respectively. **B)** DOX release profile at different pH conditions. **C)** TEM image showing the PNIPAM shell-chitosan core structure. **D)** Apatinib release profile at different temperature conditions[78]. Adapted with permission from REF. 78. Copyright (2018) Royal Society of Chemistry.

affect the diffusion behaviors of the core liquids. The benefits of understanding this are obvious. In the remote loading combined with electrospray, understanding the diffusion behavior will improve the loading efficiency, capacity, and production rate.

3) Solid-core

With electrospray, a one-step assembly of multiple functional components can be achieved instead of tedious post functionalization processes. For example, core-shell microparticles composed of a lipid shell and a core of paclitaxel (PTX)-loaded poly(lactic acid-co-glycolic acid) (PLGA) have been fabricated using co-axial electrospray (**Figure** 8A(i))[53]. The lipid layer improved particle affinity and fusion to the cell membrane for enhanced uptake (**Figure** 8A(ii)). As a result, this type of microsphere has a better anti-ovarian cancer efficacy (**Figure** 8A(iii-iv)).

Electrospray also enables one to precisely and easily control the spatial arrangement of different components in a micro/nano system. Micro/nano particles of chitosan core and polyvinylpyrrolidone (PVP) shell were prepared by electrospraying pre-mixed solution of chitosan nanoparticles and PVP polymer solution[77]. Drugs can be selectively loaded to the core or shell by adding them to chitosan or PVP, respectively, before the electrospray process. An interesting programmable dual drug release behavior was observed by switching the loading site of two model drugs from the core to shell (**Figure** 8B).

An outer solution of poly(nisopropylacylamide) (PNIPAM) containing the apatinib model drug solution and inner solution of 4-CBS-chitosan containing doxorubicin (DOX) were coaxially electrosprayed to form dual-drug loaded and dual-responsive core-shell particles with narrow size distributions (94.9±33.75 nm in diameter) (**Figure** 9)[78]. Thanks to the thermo-responsive and pH-responsive nature of PNIPAM shell and 4-CBS-chitosan core, the release rate of loaded drugs

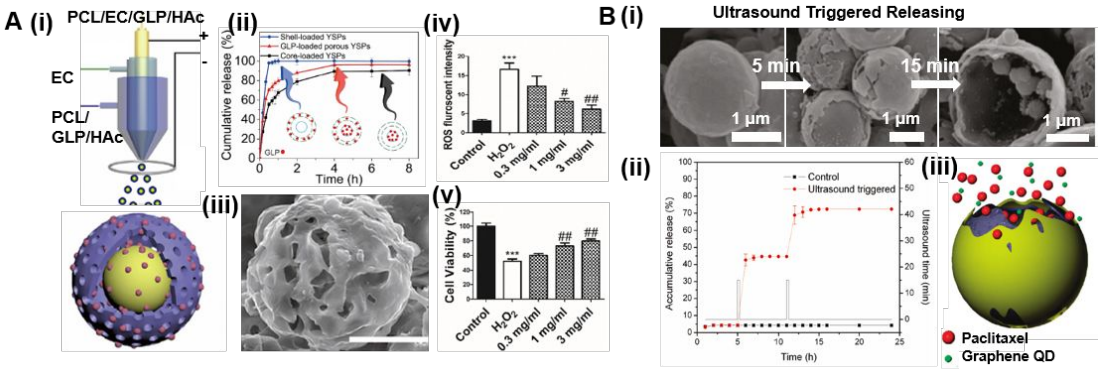

Figure 10. Preparation and characterization of yolk-shell particles. A) Ganoderma lucidum polysaccharide (GLP)-loaded PCL microparticles with porous yolk-shell structure. (i) Schematic illustration of coaxial electrospray process. (ii) Drug release profiles of particles with drug loaded in the shell only both the shell and core and core only. (iii) SEM image of the yolk-shell particle. Scale bar, 10 μm. Dependence of the (iv) intracellular reactive oxygen stress (ROS) levels and (v) cell viability on the concentration of applied yolk-shell particles[85]. ***$p < 0.001$, vs. control group; #$p < 0.05$ group vs. H_2O_2. ##$p < 0.01$ group vs. H_2O_2. Adapted with permission from REF. 85. Copyright (2018) Elsevier B.V. **B)** Imaging agent-loaded TiO_2 yolk-shell particles. (i) SEM images showing the structural change of TiO_2 yolk-shell particles with prolonged ultrasound treatment. (ii) Drug release profile under ultrasound trigger. (iii) Schematic illustration of the ultrasound-triggered release process[88]. Adapted with permission from REF. 88. Copyright (2011) American Chemical Society.

(apatinib and DOX) showed a strong dependence on pH conditions (**Figure** 9B)) and temperature (**Figure** 9A(D)). The authors show that 4-CBS-chitosan is also responsive to temperature changes. Alternative materials have to be exploited to address this problem and achieve better control over the response of the particles to different stimuli.

The yolk-shell structure can be viewed as a special version of the core-shell structure with a void space between the core and the shell. Ganoderma lucidum polysaccharide (GLP)-loaded PCL microparticles with porous yolk-shell structure (YSP) have been prepared using tri-needle coaxial electrospray (**Figure** 10A(iii))[85]. Three formulated media (GLP, PCL, and ethyl cellulose (EC) in glacial acetic acid (HAc), GLP and PCL in HAc, and EC were injected into the outer, inner, and middle compartment of the needle during the electrospray process (**Figure** 10A(i)). The benefit of such a YSP structure is two-fold. First, the core, void space, and the shell can all be exploited for loading drugs but have different drug release kinetics allowing for a multi-stage drug release that is not possible with simple, core-shell, and hollow particles[86]. **Figure** 10A(ii)) shows a porous yolk-shell structure with a biphasic drug release pattern: an initial burst release resulted from the porous shell and sustained release from the inner core. Second, the porous nature gives this particle low density, suitable aerodynamic diameter (measured to be 4.66 ± 0.25 μm), great dispersibility, and favorable lung deposition—these are all desired properties for the pulmonary route of drug administration. GLP is an active component of *Ganoderma lucidum*, which has can effectively reduce oxidative stress and thus offers therapeutic effects on chronic lung diseases[87]. After being treated with GLP-loaded porous YSPs, intracellular ROS levels showed a significant YSPs dose-dependent decrease ($p < 0.05$ for 1mg/mL YSPs and $p < 0.01$ for 3mg/mL YSPs compared to the H_2O_2-treated group) (**Figure** 10A(iv)). The MRC-5 cells were initially damaged by H_2O_2 and were subsequently treated with GLP-loaded porous YSPs of various concentrations. The cell viability increased with increasing YSPs concentrations ($p < 0.01$ for both 1mg/mL and 3mg/mL YSPs

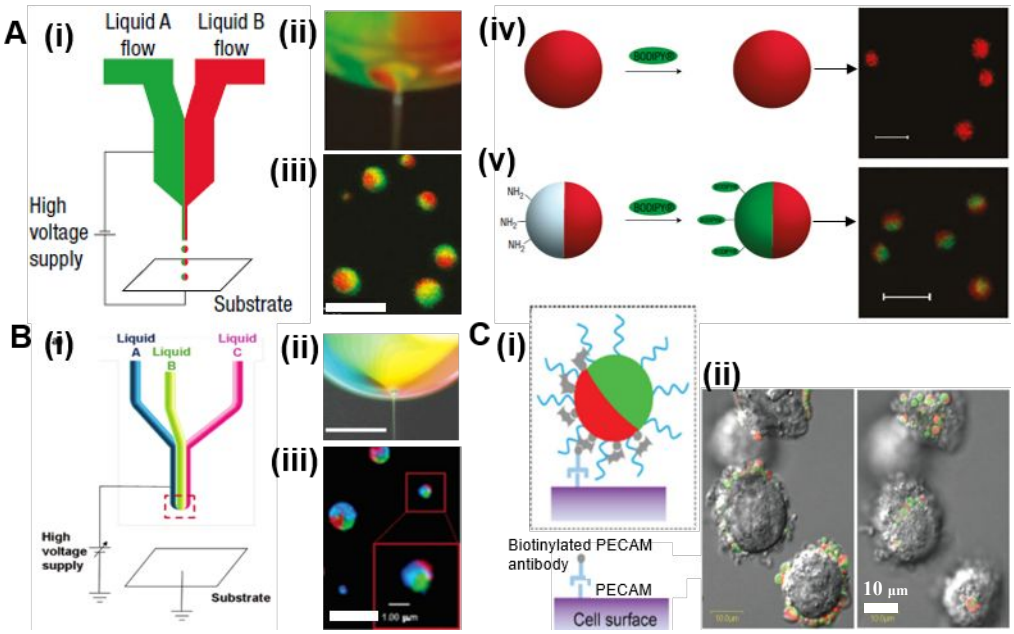

Figure 11. Preparation and characterization of Janus particles via in-parallel co-jetting electrospray. **A)** Biphasic Janus particles. (i) Experimental setup. (ii) Enlarged image showing the Taylor cone-jet mode. (iii) Confocal micrographs showing two distinct compartments. Scale bar, 4 μm. (iv) A single jetting experiment with liquid B. Only red fluorescence is observed from rhodamine B originally mixed in the jetting solution. No fluorescence from BODIPY is observed. Scale bar, 2 μm. (v) Selective chemical modification of one side of the biphasic nanoparticles. Both green fluorescent emission from BODIPY dye and red fluorescent emission from rhodamine B are observed[35]. Scale bar, 2 μm. Adapted with permission from REF. 35. Copyright (2005) Springer Nature. **B)** Triphasic Janus particles. (i) Experimental setup. (ii) Enlarged image showing the Taylor cone-jet mode. (iii) Confocal micrographs showing three distinct compartments. Scale bar, 500 μm[89]. Adapted with permission from REF. 89. Copyright (2006) American Chemical Society. **C)** Unidirectional self-assembly of biphasic Janus particles on cell surface. (i) Schematic illustration of the binding of biphasic Janus particles to cells via streptavidin present on the particle surface of one compartment and biotin from cell-specific antibody. (ii) Confocal laser scanning microscopy images taken within the same field of view at two different focal planes showing the unidirectional self-assembly process of biphasic Janus particles on the cell surface[90]. Scale bar, 10 μm. Adapted with permission from REF. 90. Copyright (2009) John Wiley & Sons Inc.

compared to the H_2O_2-treated group) (**Figure** 10A(v)). These results indicated that GLP-loaded porous YSPs are a promising treatment for chronic pulmonary diseases.

The void space in the yolk-shell structure can be utilized for the encapsulation of multifunctional components. Yolk-shell particles with drugs and imaging agents encapsulated inside a TiO_2 shell have been synthesized using coaxial electrospray (**Figure** 10B)[88]. Here, tetrabutyl titanium and PVPk-30 in ethanol, DMF, and acetic acid were in the outer solution. Paclitaxel, modified Fe_3O_4 NPs, and carbon quantum dots in olive oil were the inner solution. The inner hollow structure adds great flexibility for embedding secondary functional nanoparticles such as Fe_3O_4 NPs and carbon quantum dots for magnetic targeting and fluorescence imaging demonstrated here. The TiO_2 shell can effectively suppress the initial burst release of drugs and enables ultrasound-triggered release.

Overall, coaxial electrospray is effective for the preparation of versatile core-shell structures with

an air, liquid, and solid core. In addition to the challenges discussed following the above case studies, the size in the micro range is more common for core-shell structures. This may immediately fail applications that are size-dependent. Difficulties in reducing the size of some of the core-shell structures to the nano range are two-fold. First, the extra layers increase the overall size. Second, and more importantly, a successful preparation of these structures requires one to maintain a stable cone-jet spraying mode. Specific to a material-solvent system, there is a lower limit for the flow rate to maintain this stability. Meanwhile, the size of the particles is proportional to the flow rate. A potential solution for this could be to look into the effects of other physicochemical properties of the solution on the size as predicted by the scaling law such as solution density, electrical conductivity, surface tension, etc.

3.1.3 Janus particle

Janus particles are another type of multi-compartment particle. In contrast to the core-shell structure, compartments in Janus particles are all exposed to their environment. Synthesis of Janus particles with two (**Figure** 11A) or more (**Figure** 11B) distinct phases in a single particle using in-parallel co-jetting electrospray has been introduced[35, 89]. This approach simply injects multiple solutions in parallel and simultaneously using a multi-compartment needle during the electrospray process (**Figure** 1B), which enables a facile control over components of each phase by careful design of solutions to be sprayed. As a proof of concept, [35] electrosprayed solution mixture A (polyethylene oxide (PEO) and amino-dextran dissolved in distilled water) and B (rhodamine-B-dextran) in parallel (**Figure** 11A(i)) were sprayed and resulted in biphasic nanoparticles of two different colors (**Figure** 11A(iii)). Selective surface functionalization with BODIPY can be achieved by introducing amine groups to one of the two solutions to be electrosprayed (**Figure** 11A(v)). Green fluorescence due to BODIPY and red fluorescence due to rhodamine B were observed in each half of the particle. In contrast, no fluorescence from BODIPY is observed if the feeding solution was not treated with amine groups (**Figure** 11A(iv)).

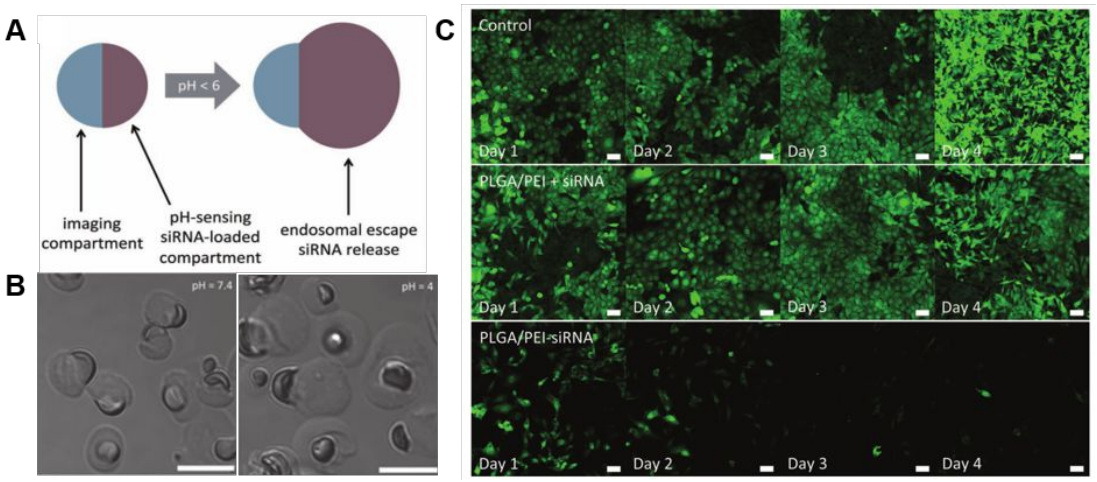

Figure 12. Preparation and characterization of Janus particles via in-parallel co-jetting electrospray continued. A) Scheme showing the biphasic Janus particle design. Two dissimilar compartments with complementary functions: imaging and siRNA delivery. **B)** Differential interference contrast microscopy showing different degrees of swelling of the PEI side at different pH levels after 6 hours of incubation in the appropriate buffered solutions. Scale bar, 10 μm. **C)** In vitro particle incubation experiments with MDA-MB-231/GFP breast cancer cells. The first row shows cells with no particle or siRNA treatment. The second row (PLGA/PEI + siRNA) shows results from incubating particles and soluble siRNA (not loaded in the particles). The third row (PLGA/PEI-siRNA)shows results from incubation with siRNA-loaded particles. Scale bar, 50 μm. The concentration of the particles shown here is 100 μg/mL[52]. Adapted with permission from REF. 52. Copyright (2012) John Wiley & Sons Inc.

Following this approach, Janus particles with various components and functions have been demonstrated. A 3-D assembly of Janus particles and cells with the spatially directed association has been achieved (**Figure** 11C)[90], which benefits from the precise conjugation of biotinylated PECAM antibody on one side of the nanoparticle.

Janus particles with PLGA on one side and polyethyleneimine (PEI) on the other have been prepared using this approach (**Figure** 12)[52]. The PLGA half-sphere is labeled with a blue fluorescent polymer dye for imaging, and the PEI half-sphere is loaded with siRNA via their counter charge interaction serving as a genetic therapeutic agent. A big challenge for the delivery of genetic materials to cells is that they will be localized in the endosomal compartment where it can be deactivated due to abundant nuclease levels and acidic pH[91]. PEI encapsulation enables siRNA to escape from endosome degradation. PEI is also pH sensitive and swells at pH=4 (**Figure** 12B), which allows for sensing of the endosomal environment, controlling the release of loaded siRNA, and even mechanical bursting out of endosome. All of these features lead to synergistic effects on silencing GFP expression as evidenced by in vitro MDA- MB-231/GFP experiments (**Figure** 12C).

Separated compartments in the Janus structure can also be exploited for loading multiple incompatible functional components in a single nanoparticle. Cadmium telluride (CdTe) quantum dots (QDs) and its quencher (PEI) have been loaded into each side of the same Janus particle (**Figure** 13A(i))[92]. This helps sustain the quantum efficiency of QDs compared to the homogenous mixing of the two (**Figure** 13A(ii)). Their release rates can be tuned separately by changing the Alg weight percentage for each compartment (**Figure** 13A(iii-v)). However, one problem that remains to be solved is the mutual diffusion of active components between the two compartments still occurred

as indicated by decreasing quantum efficiency (Figure 13A(ii)). Therefore, the selection of optimal compartmental materials that better prevent this diffusion have to be carefully considered for specific applications.

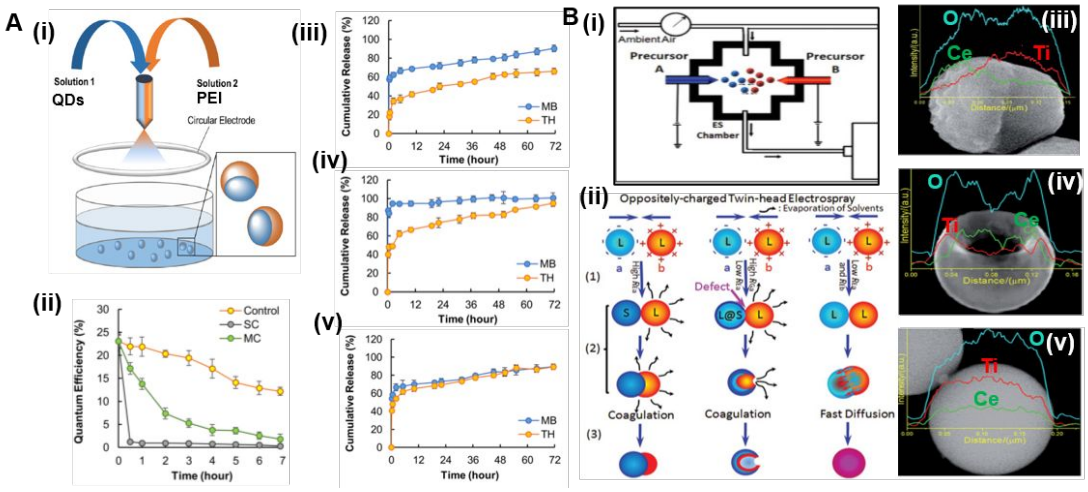

Figure 13. Preparation and characterization of Janus particles via in-parallel co-jetting electrospray continued. A) Biphasic Janus microgel with quantum dots (QDs) and PEI loaded in the two compartments separately. (i) Scheme showing fabrication of the microgel beads. (ii) Time-dependent changes in the PL quantum efficiency of the QDs co-encapsulated with PEI in the biphasic Janus microgel (MC) and single-compartment beads (SC). The QDs encapsulated in the SC beads in the absence of PEI are used as the control. Release profile of (iii) AC100 for both the methylene blue (MB)-loaded and tetracycline hydrochloride (TH)-loaded compartments, (iv) AC25 for both the MB-loaded and TH-loaded compartments, (v) AC100 for the MB-loaded compartment and AC25 for the TH-loaded compartment. The number following "AC" represents the weight percentage of Alg[92]. Adapted with permission from REF. 92. Copyright (2016) American Chemical Society. **B)** CeO_2–TiO_2 biphasic Janus particles prepared via oppositely charged twin-head electrospray. (i) Schematic illustration of the experimental setup. (ii) Scheme for the proposed formation mechanism of Janus particles. Step (1) the evaporation of solvents and gelation of precursors before the collision. Step (2) the collision and coalescence process. Step (3) the decomposition and crystallization of the precursors in post-treatment. S-L, L@S-L, and L-L collision resulted in (iii) snowman-like, (iv) pot-like, and (v) well-mixed composite particles, respectively. Here, L represents liquid droplet; S represents solid particle; L@S represents liquid core-solid shell droplet; R_{Ea} and R_{Eb} represent the evaporating rate of the solvent in droplet a and droplet b, respectively; R_{Ga} represents the gelation rate of precursor in droplet a, respectively. Inset in SEM images shown in (iii-v) represents linear EDX analysis of Ce, Ti, and O element[93]. Adapted with permission from REF. 93. Copyright (2013) Royal Society of Chemistry.

Another electrospray-based approach for the synthesis of Janus particles is oppositely charged twin-

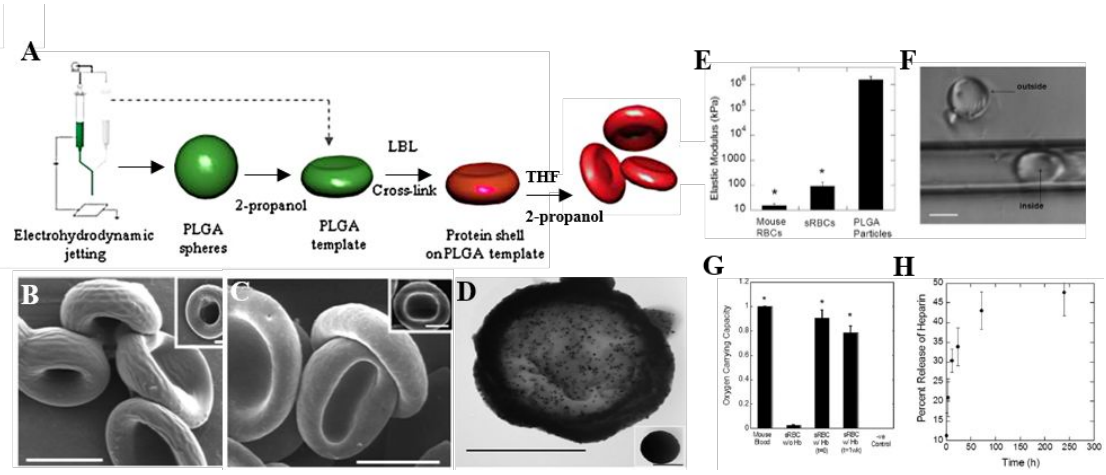

Figure 14. Preparation and characterization of Red-blood-cell-like (RBC) particles. A) Scheme for the preparation of protein sRBCs. PLGA RBC-shaped templates were synthesized by incubating spheres synthesized from electrohydrodynamic jetting in 2-propanol. Layer-by layer (LbL) coating on template, protein cross-linking, and dissolution of template core yielded biocompatible sRBCs. SEM images of **B)** biocompatible sRBCs prepared from PLGA template particles by LbL deposition of poly(allylamine hydro-chloride) (PAH)/BSA and subsequent dissolution of the polymer core and **C)** Cross-linked mouse RBCs. Scale bars, 5 μm (Insets, 2 μm). **D)** TEM image showing encapsulation of 30 nm iron oxide nanoparticles in RBC-shaped PLGA templates. The inset shows PLGA particles loaded with iron oxide nanoparticles before conversion into RBC-like templates. Scale bars, 1 μm. **E)** Comparison of elastic modulus of sRBCs with mouse RBCs and PLGA particles measured by AFM. *P<0.001, n=5. **F)** sRBCs (7 μm) flowing through glass capillary (5 μm inner diameter). Scale bar, 5 μm. **G)** Oxygen carrying capacity of sRBCs demonstrated based on the chemiluminescence reaction of luminol. Cross-linking and exposure to the organic solvent reduces the oxygen carrying capacity, but coating the sRBCs with uncross-linked Hb increased the oxygen-binding capacity to levels comparable to mouse blood (S-RBC, t=0). 90% of oxygen carrying capacity was retained after 1 week (S-RBC, t=1 wk). BSA-coated particles were included as a negative control. *P<0.01, n=3. **H)** Controlled release of radiolabeled heparin from sRBCs over a period of 10 days (n=5)[37]. Adapted with permission from REF. 37. Copyright (2009) National Academy of Sciences.

head electrospray[93]. Instead of using an in-parallel two-compartment needle, this approach features two tip-to-tip needles with the opposite charge (**Figure** 13B(i)). Two droplets were electrosprayed from two needles and coagulate into one droplet because of the Coulombic attractive forces. They then form one Janus particle after solvent evaporation and precursor gelation (**Figure** 13B(ii)). A detailed study on the effects of the chemical compositions of precursors, humidity, and concentration of solvent vapor on the morphology of CeO_2–TiO_2 oxide system has been performed, which yielded interesting structures such as snowman-like (**Figure** 13B(iii)) and pot-like (**Figure** 13B(iv)) Janus particles and well-mixed composite particles (**Figure** 13B(v)). The snowman-like CeO_2/TiO_2 Janus particle can be formed via the solid-liquid (S–L) collision where a solid TiO_2 particle collides with a liquid CeO_2 precursor droplet followed by post-heat treatment. By adjusting the hydrolysis rate, a TiO_2 precursor droplet confined by a solid shell (L@S) can be formed during the electrospray. Upon the collision with the CeO_2 precursor droplet (L@S-L collision), the pre-formed TiO_2 thin shell is damaged, and the CeO_2 precursor is deposited on the inner surface of the TiO_2 framework with a hole on the TiO_2 precursor framework forming pot-like CeO_2–TiO_2 Janus particles after heat treatment. When the evaporation rate of solvents for both droplets is significantly

decreased by increasing the solvent vapor concentration in the electrospray chamber, a liquid-liquid collision (L-L) between two droplets occur, which allows for fast diffusion and the formation of well-mixed CeO_2-TiO_2 particles (**Figure** 13B(ii)).

3.2 Non-spherical structures

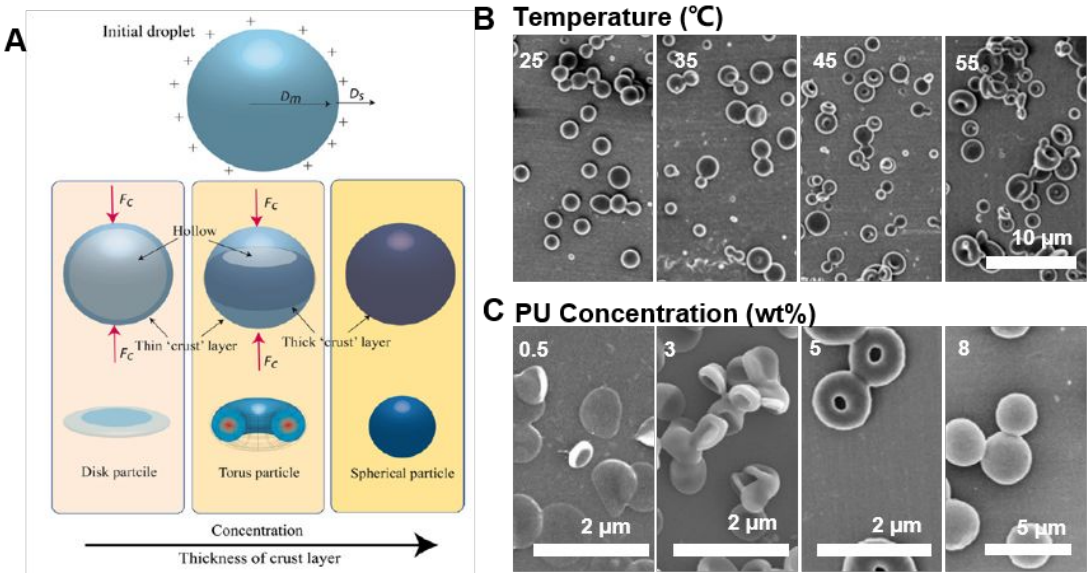

Figure 15. Preparation and characterization of RBC-like particles continued. A) Schematic of polyurethane (PU) particle shapes depending on the concentration during the consolidation of charged droplets. D_s is the diffusivity of solvents, D_m is the mutual diffusivity of solvents, F_c is the compression force. SEM images showing the dependence of PU particle shapes on **B)** temperature of electrospray environment (Scale bar, 10 μm) and **C)** PU concentration in the feeding solution for electrospray[98]. Adapted with permission from REF. 98. Copyright (2011) Elsevier Ltd.

Spherical particles are the most common type of synthetic particle due to the minimization of interfacial energy; however, non-spherical structures are more abundant in nature especially in biological systems. Indeed, the shape is not a trivial factor. For example, the shape of cells in the human body is highly related to their functions, e.g. platelets have a disc-like shape that maximizes their adhesion capability, and erythrocytes can pass through spleen filtration because of their discoid shape and flexibility[8]. The shape also plays a critical role in bacterial functions[94]. Studies have clearly shown that shape dramatically affects attachment and internalization of synthetic particles for phagocytosis and endocytosis and their circulation time in the body[10]. Specifically, the initial point of contact with the phagocyte with high curvature favors internalization[95]. Because of this, particles with extremely high aspect ratios (> 20) can largely inhibit phagocytosis because high curvature surfaces exist only at the two ends of such particles[96]. Also, elliptical discs (0.1 × 1 × 3 μm) have longer half-lives in circulation than microspheres (1–10 μm) with the same materials and coatings[97]. These features have inspired researchers to develop synthesis methods for non-spherical particles. As mentioned before, non-spherical structures achievable via electrospray include RBC-like (**Figure** 2C(i)), spindle-like (**Figure** 2C(ii))[55], multi-compartment microrods (**Figure** 2C(iii))[56], 2D holey nanosheets (**Figure** 2C(iv))[57], and nanopyramids (**Figure** 2C(v))[32]. Of these, the RBC-like structure has attracted researchers' attention and been studied more extensively due to its long circulation life, mechanical flexibility, and drug-loading and oxygen-carrying abilities[9]. In the

discussion below, we will mainly focus on RBC-like particles prepared by the electrospray method.

3.2.1 RBC-like particle

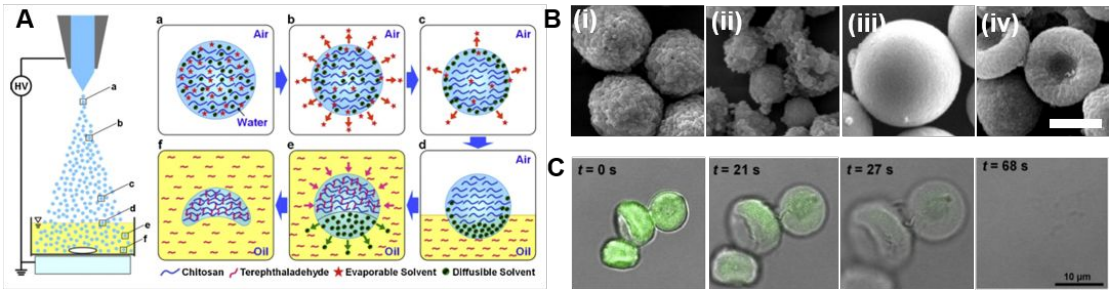

Figure 16. Preparation and characterization of RBC-like particles continued. A) Scheme for the formation mechanism of RBC-shaped chitosan microparticles. The evaporable solvent, ethanol, quickly evaporates causing a decrease in the local temperature in the droplets, which further induces the phase separation between chitosan and diffusible solvent, DMSO. As the droplets entered the oil collection medium, DMSO diffuses rapidly towards the collection solution via the water-oil interface because of high inter-solubility. Meanwhile, terephthalaldehyde in the oil phase diffuses into the droplets and crosslinks chitosan to form the RBC-like microparticles. **B)** SEM images showing the dependence of particle shapes on solvents. (i) No ethanol and DMSO, (ii) only ethanol (20 vol%), (iii) only DMSO (30 vol%), (iv) both ethanol (20 vol%) and DMSO (30 vol%). Scale bars, 5 μm. **C)** Confocal laser scanning microscope snapshots of the acid-triggered dissolution process of RBC-shaped chitosan microparticles in which pH-3.0 buffer solution is added at t = 0 s. Scale bar, 10 μm[99]. Adapted with permission from REF. 99. Copyright (2017) Elsevier B.V.

RBC-like particles are particles that mimic the unique bi-concave discoidal shape and mechanical flexibility of a real RBC. RBC-like particles can be prepared by two-step[37] or one-step electrospray[98, 99]. [37] proposed a two-step electrospray-based approach for the synthesis of RBC-like protein particles. First, the PLGA template particles were prepared through electrospray and incubated in 2-propanol to obtain the RBC-like structure. The protein shell was then coated on the PLGA RBC-like template layer-by-layer, and the template was removed (**Figure** 14A). This synthetic RBC (sRBCs) demonstrates a striking resemblance to the natural counterpart in both the morphology (**Figure** 14B-C) and properties such as mechanical softness (**Figure** 14E-F) and oxygen-carrying capacity (**Figure** 14G). The elastic modulus of sRBCs (92.8±42 kPa) was found to be four orders of magnitude lower than that of PLGA template particles (1.6±0.6 GPa) and of the same order of magnitude as that of natural RBCs. sRBCs with additional uncross-linked Hb showed comparable oxygen carrying capacity to natural mouse RBCs and 90% of oxygen carrying capacity was retained after 1 week. Moreover, sRBCs are good delivery vehicles for drugs (heparin, **Figure** 14H) and imaging agents (iron oxide NPs, **Figure** 14D).

A one-step synthesis of polyurethane (PU) sRBCs is possible by carefully controlling the electrospray environment temperature and the concentration of polymers[98]. For PU in DMF, there is a critical temperature (35 ℃) for the formation of the RBC structure (**Figure** 15B). PU concentration is another parameter to be considered: 0.5 wt% PU solutions resulted in disk-shaped particles. PU solutions at 3 wt% generated thicker disks, 5 wt% gave uniform RBC structures, and 8 wt% of polymer solutions produced spherical particles (**Figure** 15C). A PU crust layer can be formed on the surface of droplets once the concentration of polymers at the air/droplet interface reaches a critical value due to the evaporation of the solvent (**Figure** 15A). The thickness of this

crust is dependent on the concentration of the PU. A thick "crust" layer can overcome the compression force resulting from further evaporation of the solvent inside the droplet while maintaining a spherical structure; a thin crust will collapse and give a disk-shaped or RBC-like particle.

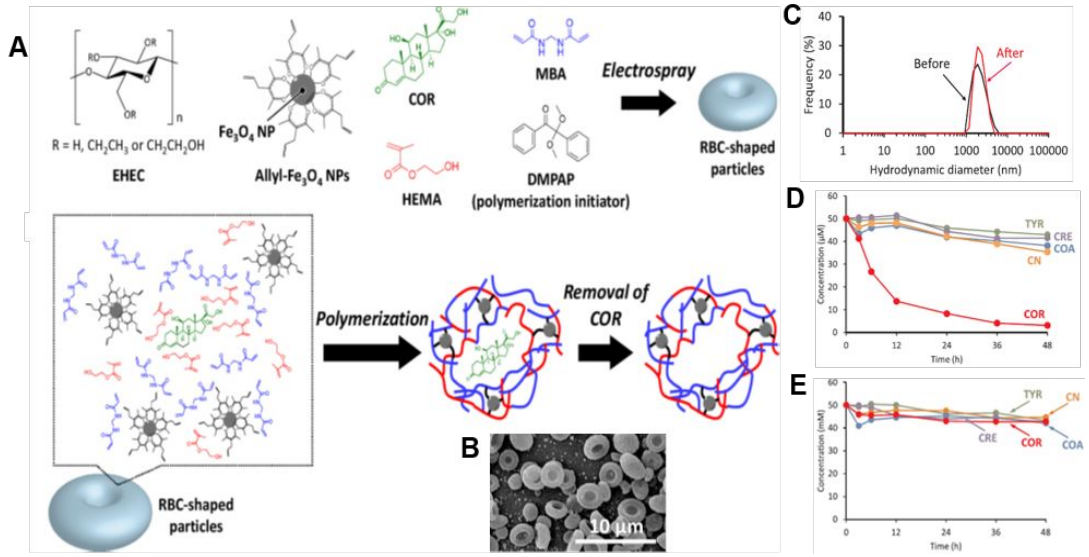

Figure 17. Preparation and characterization of RBC-like particles continued. A) Preparation scheme for RBC-shaped microparticles containing magnetite nanoparticles by electrospray combined with molecular imprinting. **B)** SEM image of as-prepared RBC-shaped microparticles containing magnetite nanoparticles. **C)** Particle size distributions of RBC-shaped particles before and after filtration through a membrane filter with pore size (1 µm) smaller than the particle size (3 µm). Concentration of cortisol (COR), creatine (CN), cholic acid (COA), creatinine (CRE), and tyrosine (TYR) in solution after immersing **D)** COR-imprinted particles and **E)** particles without COR imprinting in the solution containing these molecules[100]. Adapted with permission from REF. 100. Copyright (2018) Elsevier Ltd.

Alternatively, a one-step electrospray synthesis of RBC-like particles can be achieved by a careful selection of electrospray solvents and the collection medium. Chitosan RBC-like microparticles have been prepared by electrospraying the water phase containing chitosan polymers in ethanol and DMSO into an oil phase containing terephthalaldehyde[99] (**Figure** 16A). Once droplets are formed in the air, the evaporable solvent, ethanol, quickly evaporates, causing a decrease in the local temperature in the droplets. This further induces phase separation between chitosan and the diffusible solvent DMSO. As the droplets entered the oil collection medium, DMSO diffuses rapidly towards the collection solution via the water-oil interface because of high inter-solubility. Meanwhile, terephthalaldehyde in the oil phase diffuses into the droplets and crosslinks chitosan to form the RBC-like microparticles. **Figure** 16 B shows that a chitosan aqueous solution containing 20 vol% ethanol and 30 vol% DMSO was optimal for the preparation of RBC-like microparticles. Such particles have interesting acid-triggered dissolution and auto-fluorescence properties (**Figure** 16C).

Electrospray combined with molecular imprinting (MI) technique has been used for the preparation of ethyl(hydroxyethyl) cellulose (EHEC)-based RBC-like microparticles with a selective ability for trapping cortisol (COR) (**Figure** 17A)[100]. MI involves the creation of template-shaped cavities in

polymer matrices that is specific to the shape, size, and functional groups of the template molecules[101]. An ethanol solution containing COR, N,N'-methylenebisacrylamide (MBA), 2-hydroxyethyl methacrylate (HEMA), ethyl(hy-droxyethyl) cellulose (EHEC), 2,2-dimethoxy-2-phenylacetophenone (DMPAP), and allyl-Fe_3O_4 NPs were electrosprayed followed by the removal of the COR template and polymerization of other polymers. Such EHEC particles have great structural flexibility that enables them to pass through pore sizes (1 μm) smaller than the particle size (3 μm) (**Figure** 17C). Meanwhile, they can specifically trap COR, which is a steroid hormone produced by the adrenal glands and mainly released because of stress[102] (**Figure** 17D-E). The embedded Fe_3O_4 NPs are for magnetically capturing the microparticles with COR trapped.

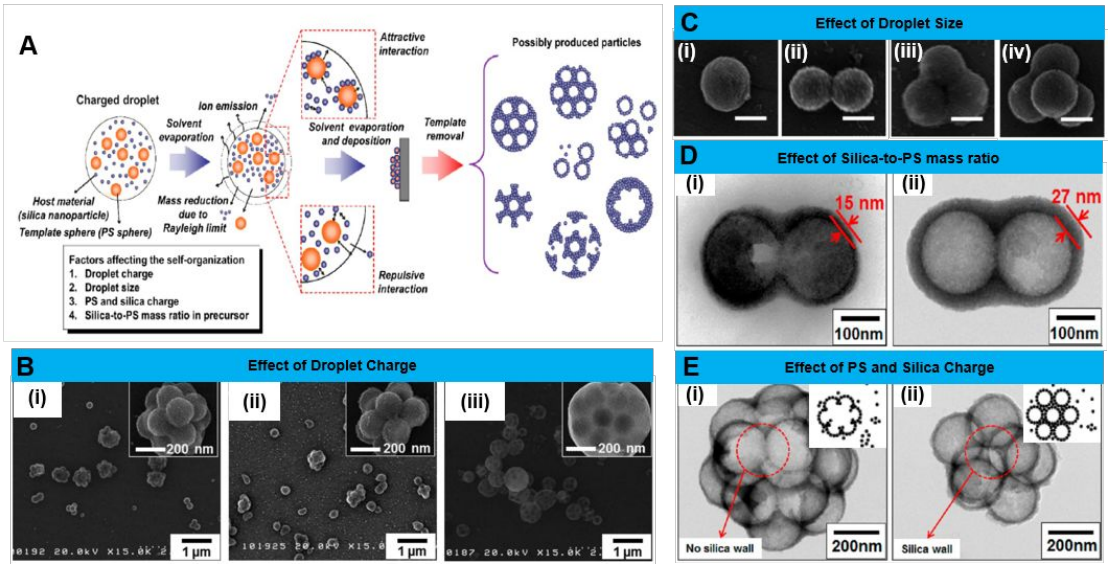

Figure 18. Self-assembly of primary building blocks in droplets formed during electrospray. A) Schematic illustration of the self-assembly process showing factors need to be considered during this process: solvent evaporation, colloid-colloid interactions, attractive and repulsive interactions between the colloidal particle and the droplet surface, ion emission, and mass reduction (Rayleigh limit theory). Dependence of the assembled structures on **B)** droplet charge, **C)** droplet size (scale bars, 200 nm), **D)** silica-to- polystyrene (PS)mass ratio, **E)** PS and silica particle charge[33]. Adapted with permission from REF. 33. Copyright (2013) American Chemical Society.

These examples show that the evaporation/diffusion of solvents governs the formation of the RBC-like structures. However, the exact mechanisms have not yet been exploited. Also, most RBC-like particles are polymer-based. Further research on the possibility of applying existing principles for the preparation of non-polymer-based RBC-like particles will definitely enrich the current materials library.

3.3 Assembled structures

The self-assembly phenomenon of colloidal particles is of fundamental scientific interest[103-106]. Self-assembly of colloidal NPs during the electrospray process has been studied systematically by [33] using silica NPs and polystyrene (PS) spheres as a model system. Specifically, the effects of droplet charge, droplet size, PS and silica NPs charge, and silica-to-PS mass ratio in electrospray liquid on the structure of the final assembly have been reported (**Figure** 18A). The charge polarity of the droplet can be controlled by the voltage generator. A positively charged droplet resulted in a

grapelike assembled structure (**Figure** 18B(i)). A negatively charged droplet gave a more irregular structure (**Figure** 18B(ii)), and a neutral droplet yielded a spherical structure with a dented surface (**Figure** 18B(iii)). Increased droplet size yielded multi spherical units in the final assembled structure (**Figure** 18C). With increasing silica/PS mass ratio, the silica shell thickness increased (**Figure** 18D). When the droplet was positively charged and silica and anionic PS were electrosprayed, no silica walls were found in the hollow particles after the removal of PS spheres (**Figure** 18E(i)). However, when silica nanoparticles and cationic PS were used, hollow particles with silica wall were produced (**Figure** 18E(ii)). This can be explained by charge-charge interaction and the Brownian motion of particles. When silica NPs and anionic PS spheres were electrosprayed, negatively charged silica NPs and PS spheres repulse each other. The positive droplet surface attracts particles. Meanwhile, the Brownian motion of the silica nanoparticles is faster than that of the PS spheres. Therefore, the outer surface of the droplet is mostly composed of silica nanoparticles while the inner is filled with continuous PS phase. However, with silica NPs and cationic PS spheres being electrosprayed, PS spheres attract surrounding silica NPs in the early stage of droplets formation, forming core−shell PS/silica nanoparticle. Extra unattached silica NPs tend to move to the outer surface of the droplet. A porous assembled structure with a clear silica wall is formed after the removal of the PS.

The significance of this work is not only limited to demonstrating versatile and interesting assembled structures based on silica and PS NPs. There must also be more general implications. First, force fields open up the opportunity to control the assembly of particles “on the fly.” Higher degrees of control over the assembled structures when the electric field is coupled with other fields, i.e., a magnetic field, may be possible. Second, the electrospray approach can significantly enrich the materials library considering that silica and PS particles can be replaced by other types of building blocks.

4. Conclusions

The advancement of nanotechnology has motivated the development of synthetic methods for micro/nano materials with precisely controlled internal structure and local composition. Despite the availability and success of versatile synthetic methods, a general “platform” approach with simplicity and scalability for the preparation of most common micro/nano structures is desired. Electrospray is a promising candidate for this purpose. Over decades of development, versatile micro/nano structures have been achieved using electrospray or electrospray combined with other methods. These include spherical structures (e.g. simple, porous, Janus, and core-shell particles), non-spherical structures (e.g. red blood cell-like and spindle-like particles, multi-compartment microrod, 2D holey nanosheet, and nanopyramid), and assembled structures of primary building blocks. Experimental approaches and underlying physical/chemical principles for the preparation of each of these categories and key benefits of such internal structures for specific applications have been reviewed in detail. The design of the nozzle is important for the synthesis of core-shell and Janus particles. Properties of feeding solutions (e.g. concentration of solute, polymer additives, solvent/nonsolvent combinations), working environment (e.g. temperature and humidity), and types of collection media have been demonstrated to be effective parameters for finely control over the pore/void formation and transition from the spherical to the non-spherical structure. Moreover, electrospray can be exploited to assemble primary building blocks, which opens more possibilities

for other interesting structures yet to be explored.

Future studies may emphasize several aspects. First, alternative strategies can be developed to control the particle size beyond the flow rate. Although the flow rate is clearly effective for this purpose within a defined size range, this method is still limited because the stability of the Taylor-cone jet spraying mode can be only maintained within a certain range of flow rate depending on the specific materials and solutions. More studies are needed to determine the effects of other solution properties on the size such as the solution density, electrical conductivity, surface tension, etc. as predicted by the scaling law.

Second, improvements are needed for the yield especially for nanoparticles. The size of the particles is proportional to the flow rate, and the synthesis of nanoparticles is usually performed under low flow rate conditions that limits the production rate. This can be potentially addressed in two ways. One can adjust other solution properties as predicted by the scaling law and find the optimal combination of these properties that favors the synthesis of nanoparticles at high flow rate conditions. Alternatively, one could scale up the number of nozzles in an electrospray system, but this requires a larger electric field, a deeper understanding of the interference of individual nozzles on the overall electric field, and a stable spray across all nozzles.

Finally, electrospray can be used to prepare advanced structures with studies of underlying physical phenomena. The electric field can be used to assemble silica and PS NPs and create versatile structures. More efforts can be directed towards the assembly of other various building blocks “on the fly.” Other forces such as magnetic force can be added by combining a magnetic field with an electric field to achieve more sophisticated control over the building blocks and advanced assembled structures.

Table. 1 Electrospray experimental details for the preparation of various structures

Structure		Matrix material	Loaded component	Particle size	Nozzle (inner diameter/gauge)	Voltage (kV)	Flowrate	Collector-to-nozzle distance (cm)	Collecting method	Ref.
Porous		Poly-L-lactide	Methotrexate	~20 μm	Simple needle (26G)	10	-	4	Ethanol bath	27
		Polyethersulfone	-	3-20 μm	Simple needle (0.5 mm)	10	1 mL/h	6	Water bath	74
		Polymethylmethacrylate	-	~5 μm	-	12	1 mL/h	12	Aluminum foil	75
Core-shell	**Air-core**	Polymethylsilsesquioxane	-	275-700 nm	Concentric needle (outer: 685 μm; inner: 150 μm)	3.5-4.5	-	1.2	Water bath	34
		Polycaprolactone (PCL)		-		-	-	-	Ethanol bath	28
	Liquid-core	Phospholipid	Tissue plasminogen activator	4-40 μm	Concentric needle (outer: 0.5 mm; inner: 0.2 mm)	0-14	Outer:48-72; inner: 9 mL/h	-	PBS bath	81
		Poly(D-lactic acid)	Hydrogel beads and dyes	~4 μm	Concentric needle (outer: 21G; inner: 23G)	9.5	Outer:8; inner: 0.4 mL/h	10	Gold-coated glass cover slip	79
		Alginate	Cell	~300 μm	Concentric needle (outer: 22G; inner: 30G)	6-11	Outer: 0.1–0.3; inner: 1–5 mL/h	12.5	Calcium chloride bath	31
		Alginate	Sucralfate	~150 μm	Concentric needle (outer: 300 μm; inner: 100 μm)	-	-	-	Calcium chloride bath	79
		Phospholipid	Resiquimod	103 nm	Concentric needle (outer: 20G; inner: 27G)	2.5	1 mL/h	0.5	PBS bath	84

Table. 1 Continued

Structure		Matrix material	Loaded component	Particle size	Nozzle (inner diameter/gauge)	Voltage (kV)	Flowrate	Collector-to-nozzle distance (cm)	Collecting method	Ref.
Core-shell	Solid-core	Core: poly (lactic acid-co-glycolic acid) (PLGA); shell: lipid	Paclitaxel	1.47 μm	Concentric needle (outer: 0.42mm; inner: 0.13 mm)	Positive: 11; negative: 8	12 uL/min	-	1% PVA solution	53
		Core: chitosan; shell: polyvinylpyrrolidone (PVP)	Naproxen & rodamine B	402/557 nm	-	16	1.5 mL/h	12	Aluminum foil	77
		Core: chitosan; shell: poly(nisopropylacylamide) (PNIPAM)	Apatinib & doxorubicin	95 nm	Concentric needle (outer: 7 mm; inner: 4 mm)	22-23	Outer: 0.1; inner: 0.3 mL/h	15	Aluminum foil	78
		Core: PLGA; shell: HSA protein	mTHPP and dasatinib	~90 nm	Simple needle (15G)	Electric field 1.5 kV/cm	-	-	Tweeen 20 aqueous solution	80
	Yolk-shell	PCL	Ganoderma lucidum polysaccharide	13.37 μm	Concentric tri-needle (outer: 2.26; middle: 1.07; innermost: 0.31 mm)	15	Outer: 5; middle: 1.5; inner: 0.8 mL/h	8	Ethanol bath	85
		TiO2	Fe3O4 NPs & carbon QDs	600 nm-6 μm	Concentric needle (size unknown)	22	Outer: 0.8; inner: 0.4 mL/h	30	-	88

Table. 1 Continued

Structure	Matrix material	Loaded component	Particle size	Nozzle (inner diameter/gauge)	Voltage (kV)	Flowrate	Collector-to-nozzle distance (cm)	Collecting method	Ref.
Janus	Polyethylene oxide	Amino-dextran & rhodamine-B-dextran	~400 nm	In-parallel needle (21G)	5-15	10 uL/h	5-25	Aluminum foil	35
	PLGA & PEI	Dyes & siRNA	216 nm &	-	-	-	-	-	52
	Alginic acid	CdTe QDs & PEI	~350 μm	-	Electric field 7 kV/cm	250 & 1000 uL/h	-	Calcium chloride bath	92
	CeO_2 & TiO_2	-	180-580 nm	Two separate simple needle	Positive: 4.5-5.5; negative:	0.1 mL/h	-	Membrane filter	93
RBC-like	PLGA	Fe3O4 NPs, protein, and heparin	~7 μm	Simple needle	5.7-6	0.7 mL/h	25-30	Aluminum foil	37
	Polyurethane	-	~4 μm	Simple needle (19G)	0-30	10 uL/h	15	Aluminum foil	98
	chitosan	-	~5 μm	Simple needle	5-6	120 uL/h	5	n-hexanol, toluene, and n-octane containing	99
	ethyl(hydroxyethyl) cellulose	COR, MBA, HEMA, DMPAP, Allyl-Fe3O4 NPs	~3 μm	Simple needle (0.6mm)	12	1 mL/h	20	-	100
Assembled	Silica NPs & PS spheres	-	~200-400 nm	Simple needle (27G)	3	1-6 uL/min	7	-	33

Conflicts of interest

There are no conflicts of interest to declare.

Acknowledgements

The authors acknowledge the support from the NSF funding under award #1845683.

We would like to thank Dr. Brendan Zhang for helpful discussions.

Reference

1. R. L. Grimm, California Institute of Technology, 2006.

2. S. Kavadiya and P. Biswas, *Journal of Aerosol Science*, 2018, **125**, 182-207.

3. L. Rayleigh, *The London, Edinburgh, and Dublin Philosophical Magazine and Journal of Science*, 1882, **14**, 184-186.

4. J. Zeleny, *Physical Review*, 1914, **3**, 69-91.

5. G. I. Taylor, *Proceedings of the Royal Society of London. Series A. Mathematical and Physical Sciences*, 1964, **280**, 383-397.

6. M. Yamashita and J. B. Fenn, *The Journal of Physical Chemistry*, 1984, **88**, 4451-4459.

7. J. W. Xie, J. Jiang, P. Davoodi, M. P. Srinivasan and C. H. Wang, *Chemical Engineering Science*, 2015, **125**, 32-57.

8. J. Cejkova and F. Stepanek, *Current Pharmaceutical Design*, 2013, **19**, 6298-6314.

9. J. W. Yoo, D. J. Irvine, D. E. Discher and S. Mitragotri, *Nat Rev Drug Discov*, 2011, **10**, 521-535.

10. S. C. Balmert and S. R. Little, *Adv Mater*, 2012, **24**, 3757-3778.

11. P. Mehta, A. Zaman, A. Smith, M. Rasekh, R. Haj-Ahmad, M. S. Arshad, S. van der Merwe, M. W. Chang and Z. Ahmad, *Advanced Therapeutics*, 2019, **2**.

12. A. D. Dinsmore, M. F. Hsu, M. G. Nikolaides, M. Marquez, A. R. Bausch and D. A. Weitz, *Science*, 2002, **298**, 1006-1009.

13. M. F. Hsu, M. G. Nikolaides, A. D. Dinsmore, A. R. Bausch, V. D. Gordon, X. Chen, J. W. Hutchinson, D. A. Weitz and M. Marquez, *Langmuir*, 2005, **21**, 2963-2970.

14. J. W. Kim, A. Fernandez-Nieves, N. Dan, A. S. Utada, M. Marquez and D. A. Weitz, *Nano Lett*, 2007, **7**, 2876-2880.

15. Y.-S. Cho, G.-R. Yi, S.-H. Kim, M. T. Elsesser, D. R. Breed and S.-M. Yang, *Journal of colloid and interface science*, 2007, **318**, 124-133.

16. H. Y. Koo, S. T. Chang, W. S. Choi, J.-H. Park, D.-Y. Kim and O. D. Velev, *Chemistry of*

Materials, 2006, **18**, 3308-3313.

17. W. Jakubowski and K. Matyjaszewski, *Macromolecules*, 2005, **38**, 4139-4146.

18. C. J. Cheng, L. Y. Chu, P. W. Ren, J. Zhang and L. Hu, *J Colloid Interface Sci*, 2007, **313**, 383-388.

19. G.-H. Ma, H. Sone and S. Omi, *Macromolecules*, 2004, **37**, 2954-2964.

20. R. Aveyard, B. P. Binks and J. H. Clint, *Advances in Colloid and Interface Science*, 2003, **100**, 503-546.

21. J. S. Hong, W. N. Vreeland, S. H. DePaoli Lacerda, L. E. Locascio, M. Gaitan and S. R. Raghavan, *Langmuir*, 2008, **24**, 4092-4096.

22. S. Liu, J. Rao, X. Sui, P. Cool, E. F. Vansant, G. Van Tendeloo and X. Cheng, *Journal of non-crystalline solids*, 2008, **354**, 826-830.

23. B. Du, Z. Cao, Z. Li, A. Mei, X. Zhang, J. Nie, J. Xu and Z. Fan, *Langmuir*, 2009, **25**, 12367-12373.

24. K. Ariga, Y. M. Lvov, K. Kawakami, Q. Ji and J. P. Hill, *Advanced drug delivery reviews*, 2011, **63**, 762-771.

25. A. J. Khopade and H. Möhwald, *Advanced Functional Materials*, 2005, **15**, 1088-1094.

26. F. Caruso, M. Spasova, A. Susha, M. Giersig and R. A. Caruso, *Chemistry of Materials*, 2001, **13**, 109-116.

27. A. Z. Chen, Y. M. Yang, S. B. Wang, G. Y. Wang, Y. G. Liu and Q. Q. Sun, *Journal of Materials Science-Materials in Medicine*, 2013, **24**, 1917-1925.

28. F. L. Zhou, A. Chirazi, J. E. Gough, P. L. H. Cristinacce and G. J. M. Parker, *Langmuir*, 2017, **33**, 13262-13271.

29. B. S. Liu, K. Nakata, M. Sakai, H. Saito, T. Ochiai, T. Murakami, K. Takagi and A. Fujishima, *Langmuir*, 2011, **27**, 8500-8508.

30. S. Y. Kim, J. Yang, B. Kim, J. Park, J. S. Suh, Y. M. Huh, S. Haam and J. Hwang, *Small*, 2013, **9**, 2325-2330.

31. D. K. Nguyen, Y. M. Son and N. E. Lee, *Advanced Healthcare Materials*, 2015, **4**, 1537-1544.

32. A. Jana, S. K. Jana, D. Sarkar, T. Ahuja, P. Basuri, B. Mondal, S. Bose, J. Ghosh and T. Pradeep, *Journal of Materials Chemistry A*, 2019, **7**, 6387-6394.

33. A. Suhendi, A. B. D. Nandiyanto, M. M. Munir, T. Ogi, L. Gradon and K. Okuyama, *Langmuir*, 2013, **29**, 13152-13161.

34. M. W. Chang, E. Stride and M. Edirisinghe, *Langmuir*, 2010, **26**, 5115-5121.

35. K. H. Roh, D. C. Martin and J. Lahann, *Nat Mater*, 2005, **4**, 759-763.

36. K. Hayashi, K. Ono, H. Suzuki, M. Sawada, M. Moriya, W. Sakamoto and T. Yogo, *Small*,

2010, **6**, 2384-2391.

37. N. Doshi, A. S. Zahr, S. Bhaskar, J. Lahann and S. Mitragotri, *Proc Natl Acad Sci U S A*, 2009, **106**, 21495-21499.

38. C. U. Yurteri, R. P. A. Hartman and J. C. M. Marijnissen, *Kona Powder and Particle Journal*, 2010, 91-115.

39. J. Zhou, D. Gao, D. Yao, S. K. Leist and Y. Fei, *International Journal of Bioprinting*, 2018, **5**.

40. S. Zhang, C. Campagne and F. Salaün, *Applied Sciences*, 2019, **9**, 402.

41. L. L. Zhang, J. W. Huang, T. Si and R. X. Xu, *Expert Review of Medical Devices*, 2012, **9**, 595-612.

42. J. A. Tapia-Hernandez, P. I. Torres-Chavez, B. Ramirez-Wong, A. Rascon-Chu, M. Plascencia-Jatomea, C. G. Barreras-Urbina, N. A. Rangel-Vazquez and F. Rodriguez-Felix, *Journal of Agricultural and Food Chemistry*, 2015, **63**, 4699-4707.

43. M. Cloupeau and B. Prunet-Foch, *Journal of Electrostatics*, 1990, **25**, 165-184.

44. M. Cloupeau and B. Prunet-Foch, *Journal of Aerosol Science*, 1994, **25**, 1021-1036.

45. H. X. Zong, X. Xia, Y. R. Liang, S. Y. Dai, A. Alsaedi, T. Hayat, F. T. Kong and J. H. Pan, *Materials Science & Engineering C-Materials for Biological Applications*, 2018, **92**, 1075-1091.

46. P. Kebarle and U. H. Verkerk, *Mass Spectrom Rev*, 2009, **28**, 898-917.

47. D. P. H. Smith, *IEEE Transactions on Industry Applications*, 1986, **IA-22**, 527-535.

48. M. Cloupeau and B. Prunet-Foch, *Journal of Electrostatics*, 1989, **22**, 135-159.

49. J. Fernández de la Mora, *Journal of Colloid and Interface Science*, 1996, **178**, 209-218.

50. A. M. GaÑÁN-Calvo, *Journal of Fluid Mechanics*, 2004, **507**, 203-212a.

51. F. Foroutan, J. V. Jokerst, S. S. Gambhir, O. Vermesh, H.-W. Kim and J. C. Knowles, *ACS Nano*, 2015, **9**, 1868-1877.

52. A. C. Misra, S. Bhaskar, N. Clay and J. Lahann, *Adv Mater*, 2012, **24**, 3850-3856.

53. P. Dwivedi, S. Y. Han, F. Mangrio, R. Fan, M. Dwivedi, Z. A. Zhu, F. S. Huang, Q. Wu, R. Khatik, D. E. Cohn, T. Si, S. Y. Hu, A. Sparreboom and R. X. Xu, *Materials Science & Engineering C-Materials for Biological Applications*, 2019, **102**, 113-123.

54. C. C. Zhang, Z. C. Yao, Q. P. Ding, J. J. Choi, Z. Ahmad, M. W. Chang and J. S. Li, *Acs Applied Materials & Interfaces*, 2017, **9**, 21485-21495.

55. D. Li, M. Marquez and Y. N. Xia, *Chemical Physics Letters*, 2007, **445**, 271-275.

56. S. Bhaskar, J. Hitt, S. W. Chang and J. Lahann, *Angew Chem Int Ed Engl*, 2009, **48**, 4589-4593.

57. D. Sarkar, B. Mondal, A. Som, S. J. Ravindran, S. K. Jana, C. K. Manju and T. Pradeep, *Global Challenges*, 2018, **2**.

58. T. K. Kim, J. J. Yoon, D. S. Lee and T. G. Park, *Biomaterials*, 2006, **27**, 152-159.

59. C. T. Bellehumeur, M. K. Bisaria and J. Vlachopoulos, *Polymer Engineering & Science*, 1996, **36**, 2198-2207.

60. Z. Pan and J. Ding, *Interface focus*, 2012, **2**, 366-377.

61. J. L. Brown, L. S. Nair and C. T. Laurencin, *Journal of biomedical materials research. Part B, Applied biomaterials*, 2008, **86**, 396-406.

62. A. I. Liapis and M. A. McCoy, *Journal of Chromatography A*, 1992, **599**, 87-104.

63. S. Haihong, L. Xiunan, M. Guanghui and S. Zhiguo, *Chromatographia*, 2005, **61**, 9-15.

64. Y. Cai, Y. Chen, X. Hong, Z. Liu and W. Yuan, *Int J Nanomedicine*, 2013, **8**, 1111-1120.

65. Y. Li, F. Gao, W. Wei, J.-B. Qu, G.-H. Ma and W.-Q. Zhou, *Journal of Molecular Catalysis B: Enzymatic*, 2010, **66**, 182-189.

66. R. Wang, Y. Zhang, G. Ma and Z. Su, *Colloids Surf B Biointerfaces*, 2006, **51**, 93-99.

67. F. Ungaro, G. De Rosa, A. Miro, F. Quaglia and M. I. La Rotonda, *European Journal of Pharmaceutical Sciences*, 2006, **28**, 423-432.

68. H. K. Kim, H. J. Chung and T. G. Park, *Journal of controlled release : official journal of the Controlled Release Society*, 2006, **112**, 167-174.

69. R. U. Agu, M. I. Ugwoke, M. Armand, R. Kinget and N. Verbeke, *Respiratory research*, 2001, **2**, 198-209.

70. M. J. Kwon, J. H. Bae, J. J. Kim, K. Na and E. S. Lee, *Int J Pharm*, 2007, **333**, 5-9.

71. E. S. Lee, M. J. Kwon, K. Na and J. H. Bae, *Colloids and surfaces. B, Biointerfaces*, 2007, **55**, 125-130.

72. D. A. Edwards, J. Hanes, G. Caponetti, J. Hrkach, A. Ben-Jebria, M. L. Eskew, J. Mintzes, D. Deaver, N. Lotan and R. Langer, *Science*, 1997, **276**, 1868.

73. S. K. Jain, G. P. Agrawal and N. K. Jain, *AAPS PharmSciTech*, 2006, **7**, 90-90.

74. Q. Zhang, J. Liu, X. Wang, M. Li and J. Yang, *Colloid and Polymer Science*, 2010, **288**, 1385-1391.

75. J. Gao, W. Li, J. S.-P. Wong, M. Hu and R. K. Y. Li, *Polymer*, 2014, **55**, 2913-2920.

76. H. F. Yang, X. Qiao, W. Hong and L. Dong, *Journal of Microelectromechanical Systems*, 2013, **22**, 509-518.

77. Y. Z. Wang, Y. Q. Zhang, B. C. Wang, Y. Cao, Q. S. Yu and T. Y. Yin, *Journal of Nanoparticle Research*, 2013, **15**.

78. H. Zhao, D. H. Sun, Y. J. Tang, J. H. Yao, X. W. Yuan and M. Zhang, *Journal of Materials Chemistry B*, 2018, **6**, 7621-7633.

79. C. Zhao, Y. R. Yu, X. X. Zhang, X. W. Wu, J. N. Ren and Y. J. Zhao, *Science Bulletin*, 2019,

64, 1418-1425.

80. R. Ramachandran, G. L. Malarvizhi, P. Chandran, N. Gupta, D. Menon, D. Panikar, S. Nair and M. Koyakutty, *Journal of Biomedical Nanotechnology*, 2014, **10**, 1401-1415.

81. W. C. Yan, Q. W. Chua, X. J. Ong, V. K. Sharma, Y. W. Tong and C. H. Wang, *J Colloid Interface Sci*, 2017, **501**, 282-293.

82. T. R. Porter and F. Xie, *Progress in Cardiovascular Diseases*, 2001, **44**, 101-110.

83. W.-s. Liu, Z.-z. Huang, X.-w. Wang and J. Zhou, *Thrombosis Research*, 2012, **130**, 547-551.

84. A. D. Duong, M. A. Collier, E. M. Bachelder, B. E. Wyslouzil and K. M. Ainslie, *Molecular Pharmaceutics*, 2016, **13**, 92-99.

85. Z. Xing, C. C. Zhang, C. Zhao, Z. Ahmad, J. S. Li and M. W. Chang, *European Journal of Pharmaceutical Sciences*, 2018, **125**, 64-73.

86. J. Liu, S. Z. Qiao, S. Budi Hartono and G. Q. Lu, *Angewandte Chemie International Edition*, 2010, **49**, 4981-4985.

87. C. Liu, N. Yang, Y. Song, L. Wang, J. Zi, S. Zhang, D. Dunkin, P. Busse, D. Weir, J. Tversky, R. L. Miller, J. Goldfarb, J. Zhan and X.-M. Li, *International Immunopharmacology*, 2015, **27**, 224-231.

88. Y. J. Jing, Y. H. Zhu, X. L. Yang, J. H. Shen and C. Z. Li, *Langmuir*, 2011, **27**, 1175-1180.

89. K. H. Roh, D. C. Martin and J. Lahann, *J Am Chem Soc*, 2006, **128**, 6796-6797.

90. M. Yoshida, K. H. Roh, S. Mandal, S. Bhaskar, D. Lim, H. Nandivada, X. Deng and J. Lahann, *Adv Mater*, 2009, **21**, 4920-4925.

91. K. A. Whitehead, R. Langer and D. G. Anderson, *Nature reviews Drug discovery*, 2009, **8**, 129-138.

92. W. F. Lai, A. S. Susha and A. L. Rogach, *Acs Applied Materials & Interfaces*, 2016, **8**, 871-880.

93. F. Z. Mou, C. R. Chen, J. G. Guan, D. R. Chen and H. Jing, *Nanoscale*, 2013, **5**, 2055-2064.

94. K. D. Young, *Current Opinion in Microbiology*, 2007, **10**, 596-600.

95. J. A. Champion and S. Mitragotri, *Proceedings of the National Academy of Sciences of the United States of America*, 2006, **103**, 4930-4934.

96. J. A. Champion and S. Mitragotri, *Pharm Res*, 2009, **26**, 244-249.

97. S. Muro, C. Garnacho, J. A. Champion, J. Leferovich, C. Gajewski, E. H. Schuchman, S. Mitragotri and V. R. Muzykantov, *Mol Ther*, 2008, **16**, 1450-1458.

98. C. H. Park, N. O. Chung and J. Lee, *J Colloid Interface Sci*, 2011, **361**, 423-428.

99. X. Ju, X. Wang, Z. Liu, R. Xie, W. Wang and L. Chu, *Particuology*, 2017, **30**, 151-157.

100. K. Hayashi, H. Hayashi, S. Yamada, W. Sakamoto and T. Yogo, *Carbohydrate Polymers*, 2018,

193, 173-178.

101. J. E. Lofgreen and G. A. Ozin, *Chemical Society Reviews*, 2014, **43**, 911-933.

102. B. S. McEwen, *New England Journal of Medicine*, 1998, **338**, 171-179.

103. N. R. Jana, *Angewandte Chemie International Edition*, 2004, **43**, 1536-1540.

104. D. Sen, O. Spalla, O. Taché, P. Haltebourg and A. Thill, *Langmuir*, 2007, **23**, 4296-4302.

105. D. Sen, S. Mazumder, J. S. Melo, A. Khan, S. Bhattyacharya and S. F. D'Souza, *Langmuir*, 2009, **25**, 6690-6695.

106. W. Liu, W. D. Wu, C. Selomulya and X. D. Chen, *Langmuir*, 2011, **27**, 12910-12915.

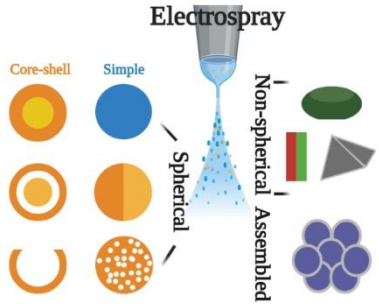

Electrospray enables the preparation of versatile spherical, non-spherical, and assembled micro/nano materials.